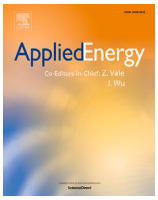
Applied Energy 418 (2026) 127974



Contents lists available at ScienceDirect

Applied Energy

journal homepage: www.elsevier.com/locate/apen



Dynamic system-level rSOC model for solar-responsive and grid-adaptive optimal operation

Maite Arce-Reyes[a,d], Felipe Huerta[a,d], Simón Díaz-Quezada[b], José R. Pérez-Correa[a], Nigel P. Brandon[c], Catalina A. Pino-Muñoz[c,*]

[a] Department of Chemical and Bioprocess Engineering, Pontificia Universidad Católica de Chile, Av. Vicuña Mackenna 4860, Macul, Santiago, 7820436, Chile
[b] Department of Chemistry and Biosciences, Aalborg Universitet, Fredrik Bajers Vej 7H, 9220, Aalborg, Denmark
[c] Department of Earth Science and Engineering, Imperial College London, London SW7 2AZ, United Kingdom
[d] UC Energy Center, Pontificia Universidad Católica de Chile, Vicuña Mackenna 4860, Macul, Santiago, 7820436, Chile

HIGHLIGHTS

- Integrated Simulink plant modelling using 1-D rSOC stack with 0-D heat transfer units.
- Continuous 24-hour cycle simulation of rSOC plant under PV intermittency.
- LHS sampling enables robust RSM surrogate models for multi-objective optimisation.
- Optimised control variables to reduce SOFC thermal gradients and improve efficiency.
- Transfer-function fitting reveals slow dynamics and strong thermal–electrical coupling.

ARTICLE INFO

Keywords:
Dynamic coupling
MATLAB/Simulink
Plant modelling
Consistent initial conditions
Multi-objective optimisation
Transfer functions
Time constants

ABSTRACT

This work presents a dynamic model of a reversible solid oxide cell (rSOC) plant operating under variable solar generation and electricity demand to enable optimal operation analysis. The model integrates a one-dimensional representation of the rSOC stack, capturing solid and gas temperatures, mass flow rates, and electrochemical performance, with zero-dimensional models of key heat-transfer units in the balance-of-plant (BoP). The innovation of this approach lies in the fully coupled framework, which combines the non-linear multi-physics of the stack with advanced physical representations of the BoP, including phase-change dynamics in the evaporator and regime-dependent heat transfer. A 24-hour simulation was performed to evaluate mode switching between solid oxide fuel cell (SOFC) and solid oxide electrolysis cell (SOEC) while tracking stack thermal stress and power. A multi-objective optimisation based on Latin Hypercube Sampling identified operating conditions that maximised electrical efficiency and reduced maximum temperature gradients in the stack. Dynamic plant analysis of a 10% step change in applied current for SOFC mode revealed that the BoP thermal inertia induces slower, more complex responses of average temperature and voltage, both displaying oscillatory behaviour. Characteristic corrected responses were fitted using parallel—first order lags and second order—transfer functions, yielding slow time constants of approximately $\tau \sim 219$ s for voltage and $\tau \sim 273$ s for average stack temperature. The similar time scales indicate the strong coupling introduced by BoP dynamics, with temperature only 1.25 times slower than voltage, contrasting with the isolated stack, where temperature responded 2.8 times slower. These findings provide a realistic framework for evaluating rSOC plants in renewable-integrated systems and support the development of advanced control strategies to ensure stable operation under intermittent energy inputs.

1. Introduction

The decarbonisation of the global energy sector relies on the rapid increase in the share of renewable energies in the energy mix. However, the integration of solar photovoltaic (PV) and wind power poses significant challenges to grid stability and energy management due to their inherent intermittency [1]. To enable more reliable operations,

* Corresponding author.
Email addresses: marce1@uc.cl (M. Arce-Reyes), fnhuerta@uc.cl (F. Huerta), sddq@bio.aau.dk (S. Díaz-Quezada), jperezc@uc.cl (J.R. Pérez-Correa), n.brandon@imperial.ac.uk (N.P. Brandon), c.pino15@imperial.ac.uk (C.A. Pino-Muñoz).

https://doi.org/10.1016/j.apenergy.2026.127974
Received 1 December 2025; Received in revised form 4 April 2026; Accepted 21 April 2026
Available online 19 May 2026
0306-2619/© 2026 The Authors. Published by Elsevier Ltd. This is an open access article under the CC BY license (http://creativecommons.org/licenses/by/4.0/).

Nomenclature

Latin

A	area, m^2
$\dot{C}$	heat capacity rate, W K^{-1}
$\hat{c}$	specific heat capacity, J $kg^{-1}K^{-1}$
C_r	heat capacity rate ratio, –
$C_{r,1/2}$	half heat capacity rate ratio, –
d	diameter, m
E	voltage, V
F	Faraday's constant, 96485 C mol^{-1}
G	transfer function, V m^2 A^{-1} or K m^2 A^{-1}
$\hat{h}$	specific enthalpy, J kg^{-1}
h	heat transfer coefficient, W m^{-2} K^{-1}
J	molar flux, mol $m^{-2}s^{-1}$
j	current density, A m^{-2}
K	steady-state gain of the system, V m^2 A^{-1} or K m^2 A^{-1}
k	thermal conductivity, W m^{-1} K^{-1}
L	length, m
l	thickness, m
$\dot{m}$	mass flow, kg s^{-1}
m	mass, kg
$\dot{n}$	molar flow rate, mol s^{-1}
N	number, –
P	power, W
p	pressure, Pa
$\dot{Q}$	heat input, W
$\dot{q}$	heat transfer rate, W
R	radiation factor, m^{-2}; resistance, Ω m^2
R_{ig}	ideal gas constant, 8.3145 J mol^{-1} K^{-1}
S	entropy, J mol^{-1} K^{-1}
s	complex frequency variable or Laplace operator, s^{-1}
T	temperature, K
t	time, s
t_s	time for onset of dynamic behaviour, s
U	global heat transfer coefficient, W m^{-2} K^{-1}
U_F	utilisation factor, –
u	velocity, m s^{-1}
$\dot{V}$	volumetric flow rate, m^3 s^{-1}
vol	volume per unit length, m^3 m^{-1}
W	molar weight, kg mol^{-1}
w	width, m
X	molar fraction, –
x	vapour quality, –
Y	mass fraction, –
y	spatial coordinate, m
y	transfer function output variable
z	spatial coordinate, m

Greek letters

β	charge-transfer coefficient, –
Δu	magnitude of the input change
Δ	change or difference
ρ	density, kg m^{-3}
ϵ	effectiveness, –
ν	stoichiometric coefficient, –
∇	gradient operator, m^{-1}
η	overpotential, V; efficiency, –
Φ	auxiliary heat exchanger function, –
ε	excess ratio, –
σ	conductivity, S m^{-1}; constant, –
τ	characteristic time constant, s; shear stress, kg m^{-1} s^{-2}
ζ	damping ratio, –

Superscripts and subscripts

0	initial state or inlet value
act	activation
ae	air electrode
amb	ambient
appl	applied
avg	average
bl	blower
c	cold
cc	counter-current
ch	channel
co	co-current
comp	compressor
conv	convective
cool	cooling
ede	electrode
eff	effective
el	electric
elyt	electrolyte
eq	equivalent
F	fuel
f	fluid
fe	fuel electrode
g	gas
h	hot
HX	heat exchanger
hyd	hydraulic
ic	interconnect
in	inlet
isen	isentropic
k	species counter
lm	log-mean
max	maximum
n	number of electrons
out	outlet
p	constant pressure
RU	repeating unit
r	reaction
rad	radiation
s	solid
sat	saturation
SB	Stefan-Boltzmann
st	stage
v	constant volume
w	wall

Abbreviations

0-D	zero-dimensional
1-D	one-dimensional
3-D	three-dimensional
ASR	area-specific resistance
BoP	balance of plant
DAE	differential algebraic equations
FESC	fuel electrode supported cell
LHS	latin hypercube sampling
LHV	lower heating value
NTU	number of transfer units
PEM	proton exchange membrane
rSOC	reversible solid oxide cell
SOEC	solid oxide electrolysis cell
SOFC	solid oxide fuel cell
TRL	technology readiness level

power systems have been designed with enhanced flexibility. This is understood as the ability to adapt generation, storage, and demand in order to compensate for fluctuations in renewable output. Energy storage and conversion technologies play an essential role in the development of flexible power systems, as they provide the capacity to mitigate fluctuations, ensure supply security, and improve overall system efficiency [2]. Within this context, reversible solid oxide cells (rSOCs) have gained increasing attention as electrochemical devices capable of operating in both fuel cell and electrolyser modes, enabling bidirectional conversion between electrical and chemical energy [3]. In electrolyser mode, they convert electricity into a fuel—typically hydrogen, which can later be used in fuel cell mode to regenerate electricity. This capability allows rSOCs to store surplus energy and supply it during periods of low renewable availability [4]. rSOCs offer higher electrical efficiency compared with low-temperature counterparts such as proton exchange membrane (PEM) fuel cells [5] and electrolysers [6]. Specifically, rSOCs operate at elevated temperatures (*ca.* 700–850 °C), achieving theoretical electrical efficiencies exceeding 70% in fuel cell mode when integrated with auxiliary thermodynamic cycles such as steam, organic Rankine, or Brayton cycles [5]. In electrolysis mode, efficiencies of 80–90% can be reached [7], and the use of residual heat further decreases the electrical energy demand during operation. Compared with the 40–50% round-trip efficiency typically reported for reversible PEM systems [8], rSOCs can reach 60–80% [8,9]. Consequently, rSOCs stand out as a promising storage technology for hybrid energy systems requiring flexibility, stability, and improved efficiency.

Several experimental demonstrations support the practical feasibility of rSOC systems coupled with renewable energy. The GrInHy project operated a Sunfire 150/30 kW rSOC system at the Salzgitter steelworks for over 5000 h in reversible mode [10,11], while [2] demonstrated stable reversible stack operation for ~1600 h under a dynamic wind-load-balancing profile. Solar and solid oxide electrolysis cell (SOEC) coupling has been demonstrated at the prototype scale by Schiller et al. [12], who integrated concentrated solar heat with steam electrolysis, and by [13], who operated a 5 kW solar steam generator connected directly to an SOEC stack. System-level studies with experimentally characterised rSOC cells further confirm the feasibility. [14] reported over 95% renewable penetration in a simulated PV–rSOC–H_2 storage minigrid. Nevertheless, a fully integrated rSOC–solar plant at scales beyond a few kilowatts has not yet been demonstrated, and significant technical challenges remain before such systems can be deployed at an industrial scale.

Despite recent progress, rSOC systems remain at a relatively low technology readiness level (TRL), typically between 5 and 7 [15], reflecting important challenges that hinder large-scale deployment. One major issue is the accelerated cell degradation, associated with mechanical failures, nickel agglomeration and migration in fuel electrodes, segregation phenomena in air electrodes, loss of contact, and electrode poisoning [16]. In addition, many of the materials currently in use were originally developed for solid oxide fuel cells (SOFCs) and show limited stability under solid oxide electrolysis cell (SOEC) conditions. Therefore, further development of materials capable of maintaining high performance and structural integrity under alternating fuel cell and electrolysis modes is essential for the advancement and widespread implementation of rSOC technology [17]. Another technical constraint is the need for safe and efficient switching between fuel cell and electrolyser modes when operating with intermittent renewable sources. These transitions involve abrupt changes in thermal, electrical, and chemical conditions that may compromise system reliability and performance [18]. While material and durability challenges remain the focus of experimental research, modelling efforts are essential to assess their impact on system performance, develop control strategies for mode switching, and support the design of reliable rSOC systems.

Currently, numerous studies focus on modelling the solid oxide cell (SOC) stack in isolation, using approaches ranging from zero-dimensional (0-D) to three-dimensional (3-D) models under both steady-state and dynamic conditions [19–23]. These detailed models capture essential phenomena such as electrochemical reactions, gas transport, and internal heat generation, and have been instrumental in improving stack design by increasing electrical efficiency and achieving more uniform temperature distributions. Wehrle et al. [24] developed a dynamic 3-D stack model, demonstrating that parameters such as the excess air ratio and voltage ramps effectively limit thermal fluctuations. Moreover, the relevance of this study lies in its analysis of the dynamic responses of temperature, current density, and species mole fractions during the transition from storage to generation. Using the $\tau_{90\%}$ criterion, they reported that the average stack temperature response exhibits a characteristic timescale of $ca.780\ s$, whereas the current density response evolves more rapidly, with $\text{ca. } 230\ s$. Although these characteristic time constants provide valuable insight into the intrinsic stack dynamics, they are not fully representative of a complete rSOC plant, since the thermal inertia of the remaining balance-of-plant (BoP) components is not captured in an isolated-stack formulation.

Building on this foundation, some recent works have begun to integrate SOC stack models with BoP components to develop more comprehensive SOC system representations. In this context, several system-level studies have adopted steady-state formulations for both the stack and the BoP components [25,26]. Buffo et al. [27] modelled an rSOC system coupled with wind power and thermal storage using steady-state submodels to analyse its operation under variable energy demand. Although the system was examined under time-varying inputs, the steady-state assumptions prevented the evaluation of characteristic time constants of the system. A similar limitation is present in the multi-scale 3-D stack representation with 0-D BoP components of [28], who examined the impact of air excess ratio and fuel utilisation on thermal gradients and efficiency. They determined that increasing the air excess ratio lowers the stack temperature gradients but also reduces both stack and system roundtrip efficiency, while a higher utilisation factor similarly decreases the thermal gradients with negligible efficiency impact. The authors also highlighted the need for future dynamic investigations to determine how BoP units influence the overall dynamic response of the stack. Reznicek and Braun [29] likewise employed a fully steady-state rSOC model, except for the storage tanks, concluding that near-ambient tank dynamics exert minimal influence on overall performance or operability, although their findings depend on the absence of dynamic interactions between the stack and the BoP. In addition to these system-level formulations, Frank et al. [30] analysed alternative rSOC plant layouts under steady-state conditions and identified an optimised configuration based on cold recirculation and internal heat recovery, achieving efficiencies of approximately 67% in SOFC mode and 76% in SOEC mode. Their analysis showed that the air flow rate governs the balance between thermal management and compressor losses, while higher fuel utilisation improves the overall efficiency when supported by recirculation. Yet, as in prior work, steady-state models cannot reveal the system's stability or its real efficiency. A proper evaluation requires accounting for the transient behaviour that appears when the stack interacts with the remaining BoP units.

Dynamic modelling efforts have attempted to overcome the limitations inherent to steady-state approaches for both the rSOC stack and the BoP. Extending the dynamic treatment to additional plant units, Liu et al. [31] developed a dynamic rSOC stack model discretised into five 0-D nodes and applied the same dynamic formulation to the heat exchangers in MATLAB/Simulink. The model captured temperature evolution over several thousand seconds during mode switching. Their analysis identified the air excess ratio as the dominant factor shaping the transient thermal response, followed by fuel utilisation and the imposed current trajectory. A similar case was reported by Xia et al. [32], who developed a dynamic 1-D SOFC system model including the stack, burner and heat exchangers, and observed non-linear thermo-electric transients under step changes in external current and stabilisation over thousands of seconds driven by the thermal capacitance of the integrated plant. Notably, the characteristic timescales obtained in these studies are approximately

three times longer than those reported by Wehrle et al. [24] for an isolated 3-D stack. Even with simplified stack representations, introducing dynamic behaviour in BoP units resulted in a significantly larger estimate of the system's effective thermal inertia.

Despite these advancements, the dynamic response of BoP components remains largely underexplored. The stack's transient response is strongly influenced by the dynamics of the surrounding equipment, and components such as heat exchangers, electric heaters, evaporators, and storage tanks play a central role in managing the flow and conditioning of reactants and products and in determining the thermal response of the system. These dynamic effects become especially critical when the plant operates under intermittent renewable energy inputs, where frequent and rapid load fluctuations occur. If BoP components are simplified under steady-state assumptions, the overall dynamic performance of the plant cannot be accurately represented, leading to an overestimation of its operational flexibility and control stability.

In parallel with the development of dynamic system models, several studies have investigated control strategies for SOC systems operating under dynamic conditions. For instance, Kim et al. [33] analysed thermal management strategies for SOEC systems during hot-standby and cold-start scenarios. In their work, the stack and selected heat exchangers were represented using dynamic 0-D models, while most BoP units were treated under steady-state assumptions. Proportional–integral (PI) controllers were implemented to regulate operating temperature and cell utilisation through electric heaters and recirculation valves. More recently, Yin et al. [34] proposed a model predictive control (MPC) strategy for regulating inlet gas temperatures in a Power-to-Gas system integrating SOEC electrolysis and methanation. In that work, the stack, heat exchangers, electric heaters and methanation reactor were represented using dynamic 0-D models, and fifth-order transfer functions were obtained using MATLAB's System Identification Toolbox based on dynamic simulations of the system. While these approaches demonstrate the importance of control strategies for safe system operation, they either rely on predefined control structures without explicitly analysing the intrinsic system dynamics or derive reduced-order models through system identification, providing limited physical insight into the integrated plant behaviour. Consequently, the characteristic time scales governing the coupled thermal–electrochemical dynamics of SOC systems remain insufficiently understood, particularly when the thermal inertia of balance-of-plant components is explicitly considered. A better understanding of these physical dynamics is therefore essential for the development of control strategies that are more robust and transferable across different operating conditions and system configurations.

In this work, we develop a system-level dynamic rSOC model capable of responding to solar generation and electricity demand profiles. The main innovation of this research is a new framework and robust numerical strategy to couple the stack's fast electrochemical phenomena with the BoP's high thermal inertia. To achieve this, the model integrates a one-dimensional (1-D) dynamic model of the rSOC stack with 0-D dynamic models for key BoP units. These BoP models incorporate advanced physical representations, such as dynamic phase-change mechanisms in the water evaporator and effectiveness-NTU formulations in the heat exchangers. The plant was simulated for continuous operation over a 24-hour duty cycle under representative current density profiles switching between SOFC and SOEC modes. To evaluate plant performance and identify optimal operating conditions, a design of experiments was conducted using a Latin Hypercube Sampling (LHS). The resulting dataset was used in a multi-objective optimisation aimed at maximising stack electrical efficiency while minimising the maximum temperature gradient across its solid layers. Finally, a time constant analysis of the stack's average temperature and cell voltage was carried out at the optimal operating point in order to characterise the dynamic behaviour of the integrated plant. By explicitly accounting for the thermal inertia of the balance-of-plant units, this analysis provides physically interpretable time constants describing the coupled thermal-electrochemical response of the rSOC system.

The remainder of this paper is organised as follows. Section 2 describes the configuration and operating principles of the rSOC plant. Section 3 presents the mathematical framework of the study, detailing the governing equations for the rSOC stack (Section 3.1), the BoP units (Section 3.2), and the numerical implementation, including discretisation techniques and simulation procedures (Section 3.3). Section 4 defines the case study, specifying the operating conditions, control variables, and parameters. Section 5 presents and discusses the results, including the validation of models, the integrated dynamic simulation of the plant, the design of experiments and multi-objective optimisation, and the determination of time constants for both the plant and the SOC stack. Finally, Section 6 summarises the main findings and provides recommendations for future work.

2. System description

The process flow diagram of the rSOC system, displaying both SOFC and SOEC operating modes, is shown in Fig. 1.

The green arrows represent pure hydrogen flow. Hydrogen stored in the tank at 7×10^6 Pa and 40 °C is extracted through stream (4) and regulated by an isoenthalpic valve, producing stream (5) at a pressure of 105,928.53 Pa. This stream is then heated in the electric heater (Heater-1) to 200 °C, generating stream (6), which is directed to the mixer. Heater-1 is included to raise the hydrogen temperature sufficiently to prevent water condensation in the mixing chamber.

Water (blue arrows) plays a dual role depending on the operating mode. In SOEC mode, water acts as a reactant and is therefore consumed in the rSOC stack. As a result, an additional supply of water from the mains (stream 22) is required to compensate for this consumption. In this case, stream (22) is active, while stream (21), which corresponds to the system water purge, remains inactive. Conversely, in SOFC mode, water is produced as a by-product of the electrochemical reaction occurring in the fuel electrode. Hence, stream (22) is inactive, and stream (21) becomes active to purge the excess water generated. The water balance point (H_2O Balance) regulates this behaviour by determining, according to the operating mode, whether water must be added to or removed from the system to form stream (1). Water is then pressurised by a pump, resulting in stream (2), which is directed to the evaporator. Inside the evaporator, the water undergoes preheating, phase change and superheating, reaching an average temperature of approximately 190 °C and a pressure of 103,851.5 Pa (stream 3). The resulting superheated steam is then mixed with the preheated hydrogen (stream 6) in the mixer, forming the fuel mixture (stream 7).

The fuel mixture (purple circuit) enters a heat exchanger (Heat Exchanger-1), where it is preheated using heat recovered from the fuel side exhaust gases leaving the stack (stream 10). If the temperature is not high enough, Heater-2 ensures that stream (8) reaches the necessary temperature before entering the stack as stream (9). After leaving Heat Exchanger-1, stream (11) still contains hydrogen and steam. This stream is fully cooled in a total condenser, where the remaining water condenses (stream 20) and the hydrogen is separated (stream 12). Both outlet streams are designed to cool down to 40 °C. The pure hydrogen stream (12) is compressed by a multistage compressor with inter-cooling (from Compressor-1 to Compressor-N) until it reaches 7×10^6 Pa and 40 °C (stream 13) to be reinjected into the hydrogen tank.

The black arrows correspond to the air supplied to the stack. Ambient air (stream 14) is driven by a blower, which delivers the pressurised stream (15) at 103,851.5 Pa. This is preheated in a plate heat exchanger (Heat Exchanger-2) using heat recovered from the air side exhaust gases leaving the stack (stream 18). This preheating reduces the thermal load on the electric heater (Heater-3), ensuring that stream (17) reaches the required operating temperature. At the stack outlet, the oxygen and nitrogen hot mixture (stream 18) enables energy recovery and leaves Heat Exchanger-2 as stream (19). This exhaust stream is then expected to be cooled down (*ca.* 40 °C) before being released to the environment.

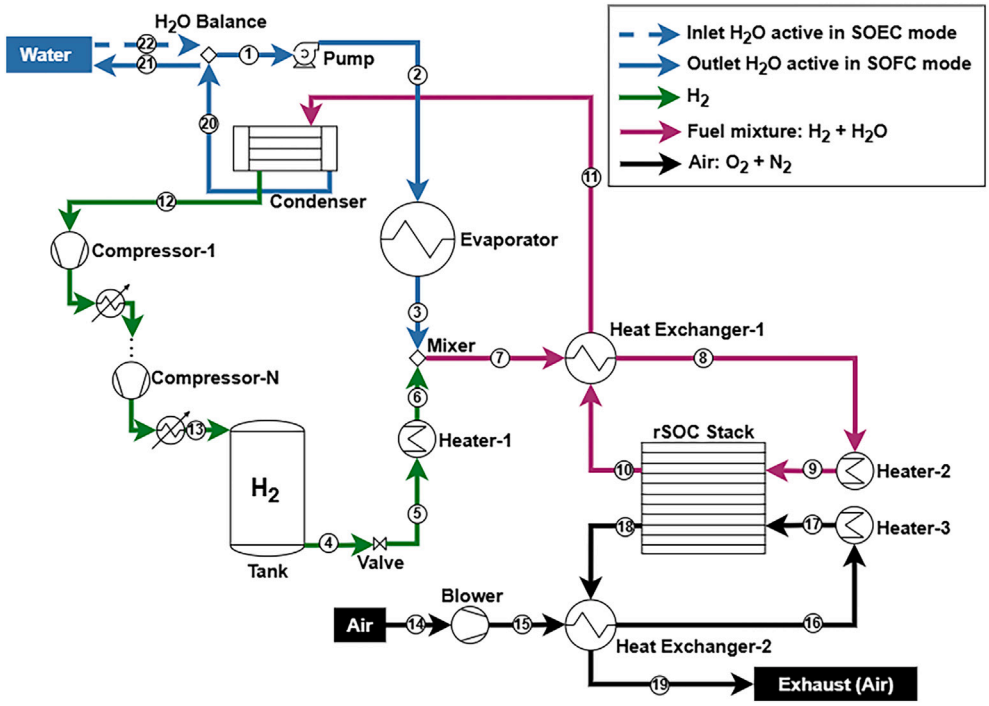


Fig. 1. Process flow diagram of the rSOC plant. Green arrows represent the hydrogen flow, blue arrows represent the water flow, purple arrows represent the fuel mixture (hydrogen and steam) flow, and black arrows represent the air flow.

The core of the system is the rSOC stack, a high-temperature electrochemical reactor. The stack consists of multiple cells electrically connected in series to achieve the desired voltage, while parallel channels ensure flow distribution. These channels are machined into interconnect plates positioned on both sides of the positive electrode-electrolyte-negative electrode (PEN) structures. This configuration enables a flow-by arrangement, with channels located above and below the electrodes to facilitate efficient transport of reactants and products. Charge-transfer reactions take place in each electrode:

Fuel electrode: $$H_{2(g)} + O^{2-}_{(elyt)} \rightleftharpoons H_2O_{(g)} + 2e^-_{(fe)}, \quad (1)$$

Air electrode: $$\frac{1}{2}O_{2(g)} + 2e^-_{(ae)} \rightleftharpoons O^{2-}_{(elyt)}, \quad (2)$$

Overall cell: $$H_{2(g)} + \frac{1}{2}O_{2(g)} \rightleftharpoons H_2O_{(g)}. \quad (3)$$

In SOFC mode, the reactions proceed forward, generating electricity and heat from the hydrogen oxidation at the fuel electrode (negative electrode) and oxygen reduction at the air electrode (positive electrode), with water produced as a by-product. Oxide ions (O^{2-}) migrate through a solid electrolyte, which separates both electrodes, while electrons circulate through an external circuit, enabling charge transfer between electrodes. In SOEC mode, the reactions reverse, consuming energy to drive water electrolysis. This energy must equal the Gibbs free energy of formation at a minimum, supplied as electricity, while the remaining enthalpy can be provided as heat to maintain the cell temperature. Depending on the operating conditions, the electrolysis process may be endothermic—requiring additional heat input—or slightly exothermic when operating above the thermo-neutral voltage, as defined by the enthalpy of formation. The electrolysis process produces hydrogen and oxygen in the fuel and air electrodes, respectively. Throughout this work, the electrodes are referred to as fuel and air electrodes instead of anode and cathode to avoid ambiguity as their roles reverse when switching between SOFC and SOEC modes.

The complete rSOC system was sized to consume approximately 500 kW in SOEC mode. The assumed cell voltages under nominal conditions were 1.22 V and 0.74 V for the SOEC and SOFC modes, respectively, at an applied current density of 0.683 A cm^{-2} corresponding to a reversible fuel electrode-supported cell (FESC) with a Ni-YSZ|YSZ|LSM-YSZ configuration [28]. The nominal power of a single rSOC stack unit (P_{stack}) was set to be *ca.* 5 kW under SOEC operation, enabling the calculation of the number of cells per stack using $P_{stack} = N_{cells/stack} E_{cell} j_{appl} A_{cell,act}$, where $N_{cells/stack}$ is the number of cells per stack, E_{cell} is the average cell voltage, j_{appl} is the applied current density, and $A_{cell,act}$ is the active area of a single cell. Accordingly, the number of stacks was selected to meet the total electrical power demand of the rSOC system. Given these conditions, the nominal power output in SOFC mode was lower, about 3 kW per stack. The nominal electrochemical parameters used in the stack design are summarised in Table A.1. Geometrical parameters for the Positive electrode-Electrolyte-Negative electrode (PEN) structure and stack, as well as the number of stacks considered in the plant, are detailed in Table A.2. The specific design characteristics of the FESC, including PEN configuration and electrode parameters, are reported by Wang et al. [28].

3. Computational methods

3.1. Reversible solid oxide cell modelling

The implementation of the dynamic stack model is based primarily on established and widely adopted formulations in the literature [19,20,28,30,35]. These models have been extensively validated and serve as a standard foundation for the model developed in this work. Table 1 summarises the governing partial differential equations (PDEs) and boundary conditions. Details on the electrochemical model and property calculations can be found in the Supplementary Information. The full list of symbols and abbreviations is provided in the Nomenclature section for clarity and reference. The model details and main assumptions considered are as follows:

(i) A planar insulated stack placed in ambient surrounding conditions is considered. Co-flow configuration is assumed for the gas

Table 1
Summary of governing PDEs and boundary conditions in the one-dimensional rSOC model.

Physico-chemical process Domain	Model equation	Eq.
Momentum conservation Gas channels	$\frac{\partial(\rho_g u)}{\partial t} + \frac{\partial(\rho_g uu)}{\partial z} = -\frac{\partial p}{\partial z} - \frac{4\tau_w}{d_{hyd}}$ s.t. $u\|_{z=0} = u^{in}$ and $\left.\frac{du}{dz}\right\|_{z=L_{ch}} = 0$	(4)
Mass conservation Gas channels - total	$\frac{\partial \rho_g}{\partial t} + \frac{\partial(\rho_g u)}{\partial z} = \frac{1}{l_{ch}} \sum_k (J_k W_k)$, for $k \in \begin{cases} \{O_2, N_2\} & \text{in air electrode} \\ \{H_2, H_2O\} & \text{in fuel electrode} \end{cases}$ s.t. $\rho_g\|_{z=0} = \rho_g^{in}$ and $\left.\frac{d\rho_g}{dz}\right\|_{z=L_{ch}} = 0$	(5)
Gas channels - species	$\frac{\partial(\rho_g Y_k)}{\partial t} + \frac{\partial(\rho_g u Y_k)}{\partial z} = \frac{1}{l_{ch}} J_k W_k$, for $k \in \begin{cases} \{O_2, N_2\} & \text{in air electrode} \\ \{H_2, H_2O\} & \text{in fuel electrode} \end{cases}$ s.t. $Y_k\|_{z=0} = Y_k^{in}$ and $\left.\frac{dY_k}{dz}\right\|_{z=L_{ch}} = 0$	(6)
Energy conservation Gas channels	$\frac{\partial(\rho_g \hat{c}_{v,g} T_g)}{\partial t} + \frac{\partial(u \rho_g \hat{c}_{p,g} T_g)}{\partial z} = \frac{h_{conv}}{l_{ch}}(T_{ede} - T_g) + h_{conv}(T_{ic} - T_g)\left(\frac{2l_{ch} + w_{ch}}{w_{ch} l_{ch}}\right)$ s.t. $T_g\|_{z=0} = T_g^{in}$ and $\left.\frac{dT_g}{dz}\right\|_{z=L_{ch}} = 0$	(7)
Fuel electrode	$\rho_{fe}^{eff} \hat{c}_{p,fe}^{eff} \frac{\partial T_{fe}}{\partial t} = k_{fe}^{eff} \frac{\partial^2 T_{fe}}{\partial z^2} - \frac{h_{conv}}{l_{fe}}(T_{fe} - T_g)\left(\frac{w_{ch}}{w_{RU}}\right) + \frac{j_{appl}^2}{\sigma_{fe}^{eff}} - \frac{\sigma_{SB}(T_{fe}^4 - T_{ic,fe}^4)}{R_{rad,ic->ede} l_{fe}}\left(\frac{1}{w_{RU}}\right) + \frac{j_{appl}}{l_{fe}}\left(\eta_{act,fe} - \frac{T_{fe}\Delta S_{r,fe}}{nF}\right) + \frac{\dot{q}_{fe}}{w_{ch} L_{ch}\left(l_{fe}/2 + l_{elyt}/2\right)}$ s.t. $-k_{fe}^{eff}\left.\frac{\partial T_{fe}}{\partial z}\right\|_{z=0} = \frac{T_{amb} - T_{fe}}{R_{eq}}$ and $-k_{fe}^{eff}\left.\frac{\partial T_{fe}}{\partial z}\right\|_{z=L_{ch}} = \frac{T_{fe} - T_{amb}}{R_{eq}}$	(8)
Electrolyte	$\rho_{elyt} \hat{c}_{p,elyt} \frac{\partial T_{elyt}}{\partial t} = k_{elyt} \frac{\partial^2 T_{elyt}}{\partial z^2} + \frac{j_{appl}^2}{\sigma_{elyt}} + \frac{\dot{q}_{fe}}{w_{ch} L_{ch}\left(l_{fe}/2 + l_{elyt}/2\right)} - \frac{\dot{q}_{ae}}{w_{ch} L_{ch}\left(l_{ae}/2 + l_{elyt}/2\right)}$ s.t. $-k_{elyt}\left.\frac{\partial T_{elyt}}{\partial z}\right\|_{z=0} = \frac{T_{amb} - T_{elyt}}{R_{eq}}$ and $-k_{elyt}\left.\frac{\partial T_{elyt}}{\partial z}\right\|_{z=L_{ch}} = \frac{T_{elyt} - T_{amb}}{R_{eq}}$	(9)
Air electrode	$\rho_{ae}^{eff} \hat{c}_{p,ae}^{eff} \frac{\partial T_{ae}}{\partial t} = k_{ae}^{eff} \frac{\partial^2 T_{ae}}{\partial z^2} - \frac{h_{conv}}{l_{ae}}(T_{ae} - T_g)\left(\frac{w_{ch}}{w_{RU}}\right) + \frac{j_{appl}^2}{\sigma_{ae}^{eff}} - \frac{\sigma_{SB}(T_{ae}^4 - T_{ic,ae}^4)}{R_{rad,ic->ede} l_{ae}}\left(\frac{1}{w_{RU}}\right) + \frac{j_{appl}}{l_{ae}}\left(\eta_{act,ae} - \frac{T_{ae}\Delta S_{r,ae}}{nF}\right) - \frac{\dot{q}_{ae}}{w_{ch} L_{ch}\left(l_{ae}/2 + l_{elyt}/2\right)}$ s.t. $-k_{ae}^{eff}\left.\frac{\partial T_{ae}}{\partial z}\right\|_{z=0} = \frac{T_{amb} - T_{ae}}{R_{eq}}$ and $-k_{ae}^{eff}\left.\frac{\partial T_{ae}}{\partial z}\right\|_{z=L_{ch}} = \frac{T_{ae} - T_{amb}}{R_{eq}}$	(10)
Interconnects	$\rho_{ic}^{eff} \hat{c}_{p,ic} \frac{\partial T_{ic}}{\partial t} = k_{ic} \frac{\partial^2 T_{ic}}{\partial z^2} - h_{conv}(T_{ic} - T_g)\left(\frac{2l_{ch} + w_{ch}}{vol_{ic}}\right) + \frac{\sigma_{SB}(T_{ede}^4 - T_{ic}^4)}{R_{rad,ic->ede}}\left(\frac{1}{vol_{ic}}\right)$ s.t. $-k_{ic}\left.\frac{\partial T_{ic}}{\partial z}\right\|_{z=0} = \frac{T_{amb} - T_{ic}}{R_{eq}}$ and $-k_{ic}\left.\frac{\partial T_{ic}}{\partial z}\right\|_{z=L_{ch}} = \frac{T_{ic} - T_{amb}}{R_{eq}}$	(11)

channels built into the bipolar interconnects at each side of the positive electrode-electrolyte-negative electrode (PEN) cells.

(ii) The rSOC stack was modelled considering a representative interconnect-channel-PEN unit. The model comprises a transient 1-D gas transport model in channels and transient 1-D heat transport models in channels, PEN (electrodes and electrolyte) and interconnects along the axial direction, coupled to a steady-state 1-D model across the PEN (transverse direction).

(iii) A 1-D heat transport model is selected as the solid stacks temperature gradients are expected to appear mostly in the axial direction when a 3-D insulated stack is simulated as reported by [19,36].

(iv) Flow dynamics in the stack inlet and outlet manifolds are not considered.

(v) In the channels, the gas flow is considered to be 1-D and laminar, which is a good approximation for channels with small characteristic diameters (<1 cm) and low mean velocities (<100 cm s^{-1}) [36,37]. Only convective axial transport is considered, while axial diffusion is neglected due to the high aspect ratio of the channels and the low axial diffusion velocities [19,36,37]. The gas heat transport is convective in the axial direction and includes convective heat sources due to heat transfer between the gas and channel surfaces (interconnect and electrode).

(vi) For the solid stack, conductive heat transport is considered to be 1-D for each component in the PEN and interconnects. Convective heat transfer is considered between the solid surfaces and gases in the channels. Radiative heat transfer is present between the interconnect and electrode surfaces delimiting the channels and is considered to be diffuse, opaque and gray. Conductive heat transfer between adjacent PEN components is included. Additionally, electrodes' heat sources include Joule heating due to current conduction through electrodes, electrochemical reversible heat due to the reactions' entropy change and irreversible heat due to activation overpotentials.

(vii) Gas species transport in the PEN is considered steady 1-D through the thickness of the electrodes, with charge transfer reactions occurring throughout the electrodes lumped into fluxes at the electrode-electrolyte interfaces. Therefore, electronic and ionic potentials across the electrodes are not solved.

(viii) Gas species fluxes through electrodes are described by a Fick model considering an effective diffusivity, which accounts for Knudsen and molecular diffusion

coefficients and is a function of the electrode's porosity and tortuosity.

(ix) The charge transfer kinetics in both electrodes are described by global Butler-Volmer (BV) kinetics using empirical power laws to express the exchange current densities dependence on gas species.

(x) The electrode area underneath the interconnect rib was assumed to be electrochemically inactive. Only the electrode area underneath the channel was considered for the charge-transfer reaction.

(xi) Material properties of PEN components are considered constant and homogeneous.

(xii) The dense electrolyte is considered an electronic insulator, therefore only ionic charge transport is present with no leakage current.

(xiii) Current collection at interconnects is considered perfect and no contact resistance is assumed.

3.2. Balance of plant modelling

The BoP units were represented using dynamic or steady-state thermodynamic models. The main assumptions considered are as follows:

(i) All auxiliary heat-transfer units were modelled using a 0-D approach for the energy balances. To ensure thermodynamic consistency and prevent unphysical temperature crossings, the heat exchangers (HX) were implemented using the effectiveness-NTU (ε-NTU) method based on the VDI Heat Atlas [38] for a specific flow arrangement (1-pass for the hot stream and 2-passes for the cold stream). This formulation, originally derived by Kandlikar and Shah [39], calculates outlet temperatures as a weighted assembly of counter-current and co-current flow regimes. The mass balances were assumed to be in a steady state. The only exceptions were the inter-cooling heat exchangers of the multi-stage compressor and the condenser. No reactions take place in the BoP units and accumulation effects that may appear during step changes were assumed to disappear almost immediately compared to thermal transients. Consequently, the inlet and outlet mass flow rates are equal, and species concentrations remain constant throughout each unit.

(ii) The hydrogen tank was dynamically modelled through a 0-D formulation for both mass and energy balances, following the approach of [29].

(iii) The compressor, blower and hydraulic pumps were modelled in steady state because their dynamic response is significantly faster than the dynamics of the stack and the thermal units of the plant [40,41]. The reported time constants are of the order of $\tau_{\text{comp}} \sim 3$ s for hydrogen compressors [42], $\tau_{\text{blower}} \sim 0.3$ s for blowers [43], and $\tau_{\text{pump}} \lesssim 0.05$ s for hydraulic pumps [44].

(iv) Isentropic efficiencies of 85% were assumed for both the blower and the compressors [45], with no additional mechanical-loss corrections. The pumps were modelled using a hydraulic efficiency of 54%, representing an overall efficiency that already includes the isentropic and mechanical loss mechanisms [27].

(v) All heat transfer units were modelled as adiabatic, neglecting heat losses to the surroundings. Their shells were assumed to be thin and covered with highly efficient thermal insulation. The hydrogen tank accounted for the heat losses to the surroundings, considering an ambient temperature of 25 °C.

(vi) Internal pressure drops were not explicitly modelled. A mean pressure loss of 500 Pa was assumed in the heat exchangers [27], and a 2% pressure reduction was applied to the remaining auxiliary units [46]. Pressure drops along the connecting pipelines were also neglected.

(vii) The expansion valve was modelled as an isenthalpic component to capture the temperature variation associated with the Joule–Thomson (JT) effect [47].

(viii) The mixing of gases was considered to occur under adiabatic conditions, allowing the calculation of the composition and temperature of the gas mixture leaving the Mixer.

The governing equations for the BoP units are presented in Table 2. For the compact plate-type heat exchangers, the temperatures of both gaseous streams (Eqs. (12) and (13)) and the wall (Eq. 14) are dynamically solved.

The evaporator was dynamically modelled using a 0-D formulation that accounts for the phase change of water. The energy balance was expressed in terms of the specific enthalpy of the fluid (Eq. 27), allowing the instantaneous vapour quality (Eq. 29) to be determined and the heat transfer coefficients to be updated according to the thermal regime (subcooled, two-phase, or superheated). The average temperature of the metallic wall was also modelled (Eq. 28), while the heating fluid was assumed to be air at 200 °C.

All heat-transfer correlations employed in the plate-type heat exchangers and in the evaporator—including regime-dependent formulations for gases, liquid water, and two-phase mixtures—are compiled in the Supplementary Information.

In the case of electric heaters, both the fluid and wall temperatures were modelled (Eqs. (30) and (31), respectively), assuming a constant heat source capable of achieving the target inlet temperature to the stack. This approach captures the thermal inertia of the metal without explicitly implementing electrical control.

The multi-stage hydrogen compressor (Eq. 37) includes intercoolers operating under steady-state conditions after each compression stage (Eq. 38). A maximum outlet-gas temperature of 135 °C was imposed for every stage, in accordance with the API Guideline 618 for hydrogen-rich gases [48], which provides safety recommendations for reciprocating compressors. The intercoolers prevent the hydrogen temperature from approaching its autoignition limit (585 °C [49]) and ensure a final-stage outlet temperature of 40 °C. Given these requirements, the multi-stage hydrogen compressor was designed with 5 compression–intercooling stages.

The dynamic BoP components were thermally sized according to the operating requirements of the rSOC plant. The plate type heat exchangers and the evaporator were designed using the NTU $-\varepsilon$ method, ensuring that during SOFC operation at the maximum current density ($j_{\text{appl}} = 4829.07$ A m^{-2}) the outlet gas temperatures reached the target values without activating electric heaters. Conversely, the electric heaters were sized based on the most demanding SOEC condition, corresponding to a current of -6218.55 A m^{-2}. The hydrogen storage tank was sized by estimating the mass required to sustain four hours of SOFC operation at nominal conditions.

To improve numerical robustness, polynomial correlations were fitted for the specific heat capacities and enthalpies of each working fluid using data from COOLPROP [50]. These correlations were implemented in all heat transfer units to ensure smooth property variations during dynamic simulations.

3.3. Numerical implementation

The dynamic model of the rSOC stack was implemented in MATLAB using the method of lines. The governing equations for mass, momentum, species, and energy conservation in the gas channels, electrodes, electrolyte, and interconnects were discretised along the axial coordinate with finite difference schemes. Convective terms were approximated with a first order upwind scheme and diffusive terms with a second order central scheme. This spatial discretisation transforms the system of partial differential equations into a set of coupled differential

Table 2
Governing equations related to the modelling of the BOP components in MATLAB.

Component	Governing equations	Eq.
Heat exchangers	$\frac{dT_c}{dt} = \frac{\dot{m}_c \hat{c}_{p,c}\left(T_c^{in} - T_c^{out}\right) + A_{transfer}\, h_{conv,c}\left(T_w - T_c\right)}{m_c \hat{c}_{p,c}}$	(12)
	$\frac{dT_h}{dt} = \frac{\dot{m}_h \hat{c}_{p,h}\left(T_h^{in} - T_h^{out}\right) - A_{transfer}\, h_{conv,h}\left(T_h - T_w\right)}{m_h \hat{c}_{p,h}}$	(13)
	$\frac{dT_w}{dt} = \frac{A_{transfer}\, h_{conv,h}\left(T_h - T_w\right) - A_{transfer}\, h_{conv,c}\left(T_w - T_c\right)}{m_w \hat{c}_{p,w}}$	(14)
Outlet Hot	$T_h^{out} = T_h^{in} - \epsilon_{HX}\left(T_h^{in} - T_c^{in}\right)$	(15)
Outlet Cold	$T_c^{out} = T_c^{in} + C_r \epsilon_{HX}\left(T_h^{in} - T_c^{in}\right)$	(16)
Heat Capacity Rates	$\dot{C}_h = \dot{m}_h \hat{c}_{p,h} \quad ; \quad \dot{C}_c = \dot{m}_c \hat{c}_{p,c}$	(17)
Capacity Ratio	$C_r = \frac{\dot{C}_h}{\dot{C}_c} \quad ; \quad C_{r,1/2} = \frac{C_r}{2}$	(18)
Transf. Units	$NTU = \frac{UA}{\dot{C}_h}$	(19)
Effectiveness (ϵ_{HX})	$\epsilon_{HX} = 0.5\left(\Phi_{cc} + \Phi_{co} - 0.5 C_r \Phi_{cc}\Phi_{co}\right)$	(20)
Counter-current (Φ_{cc})	$\Phi_{cc} = \frac{1 - \exp[-NTU(1 - C_{r,1/2})]}{1 - C_{r,1/2}\exp[-NTU(1 - C_{r,1/2})]}$	(21)
Co-current (Φ_{co})	$\Phi_{co} = \frac{1 - \exp[-NTU(1 + C_{r,1/2})]}{1 + C_{r,1/2}}$	(22)
Heat transfer rates	$\dot{Q}_{h\to w} = h_h A_{transfer}(T_h^{avg} - T_w); \quad \dot{Q}_{w\to c} = h_c A_{transfer}(T_w - T_c^{avg})$	(24)
Driving Force	$\Delta T_{lm} = \frac{\left(T_h^{in} - T_c^{out}\right) - \left(T_h^{out} - T_c^{in}\right)}{\ln\left(\frac{T_h^{in} - T_c^{out}}{T_h^{out} - T_c^{in}}\right)}$	(25)
Heat Loss	$\dot{Q}_{loss} = 0$ (Adiabatic Assumption)	(26)
Evaporator	$\frac{d\hat{h}_{H_2O}}{dt} = \frac{\dot{m}_{H_2O}\left(\hat{h}_{H_2O}^{in} - \hat{h}_{H_2O}^{out}\right) + A_{transfer}\, h_{conv,H_2O}\left(T_w - T_{H_2O}\right)}{m_{H_2O}}$	(27)
	$\frac{dT_w}{dt} = \frac{A_{transfer}\, h_{conv,h}\left(T_h - T_w\right) - A_{transfer}\, h_{conv,H_2O}\left(T_w - T_{H_2O}\right)}{m_w \hat{c}_{p,w}}$	(28)
	$x = \frac{\hat{h}_{H_2O} - \hat{h}_{H_2O,l}^{sat}}{\Delta \hat{h}_{lg}}$	(29)
Electric Heaters	$\frac{dT_f}{dt} = \frac{h_{conv} A_{transfer}\left(T_w - T_f\right) + \dot{m}_f \hat{c}_{p,f}\left(T_f^{in} - T_f^{out}\right)}{m_f \hat{c}_{p,f}}$	(30)
	$\frac{dT_w}{dt} = \frac{\dot{Q}_{electric} - h_{conv} A_{transfer}\left(T_w - T_f\right)}{m_w \hat{c}_{p,w}}$	(31)
Hydrogen Tank	$\frac{dn_{H_2}}{dt} = \dot{n}_{H_2}^{in} - \dot{n}_{H_2}^{out}$	(32)
	$\frac{d\left(n_{H_2}\hat{h}_{H_2}\right)}{dt} = \dot{n}_{H_2}^{in}\hat{h}_{H_2}^{in} - \dot{n}_{H_2}^{out}\hat{h}_{H_2}^{out} - A_{transfer}\, h_{amb}\left(T_{H_2} - T_{amb}\right)$	(33)
Pump	$P_{pump} = \frac{\dot{V}_{H_2O}\left(p_{H_2O}^{out} - p_{H_2O}^{in}\right)}{\eta_{hyd}}$	(34)
Valve	$\hat{h}_{H_2}\left(T_{H_2}^{out}, p_{H_2}^{out}\right) = \hat{h}_{H_2}\left(T_{H_2}^{in}, p_{H_2}^{in}\right)$	(35)
Blower	$P_{bl} = \frac{\dot{m}_{air}}{\eta_{isen}}\left(\hat{h}_{air}^{out,isen} - \hat{h}_{air}^{in}\right)$	(36)
Multi-stage Compressor	$P_{comp} = \frac{\dot{m}_{H_2}}{\eta_{isen}}\sum_{i=1}^{N_{st}} \hat{c}_{p,H_2,i}\left[T_{H_2,i}^{out,isen} - T_{H_2,i}^{in}\right]$	(37)
Intercoolers	$\dot{Q}_{cool} = \dot{m}_{H_2}\left(\hat{h}_{H_2}^{out} - \hat{h}_{H_2}^{target}\right)$	(38)
Condenser	$\dot{Q}_{condenser} = \dot{m}_{fuel}\left[\left(\hat{h}_{fuel,g}^{in} - \hat{h}_{fuel,g}^{sat}\right) + w_{H_2O}\left(\hat{h}_{H_2O,g}^{sat} - \hat{h}_{H_2O,l}^{sat}\right) + w_{H_2}\left(\hat{h}_{H_2,g}^{sat} - \hat{h}_{H_2,g}(T_{target})\right) + w_{H_2O}\left(\hat{h}_{H_2O,l}^{sat} - \hat{h}_{H_2O,l}(T_{target})\right)\right]$	(39)

algebraic equations (DAEs). The activation overpotentials in electrodes, which influence energy source terms, were calculated from implicit Butler–Volmer expressions that depend on the local temperature, gas composition, and applied current density. The semi-discretised system was integrated in time using the variable-step, variable-order MATLAB solver `ode15s`. This solver enforces the algebraic constraints at each time step through an internal implicit iteration.

The initial conditions for all solid and gaseous domains in the rSOC stack model were defined consistently across the computational domain. The initial temperatures of the solid structures, including electrodes, electrolyte, and interconnects, were set equal to the inlet gas temperature (T_g^0, K) entering the fuel and air channels. The initial gas densities (ρ_g^0, kg m^{-3}) were calculated from the corresponding initial pressure (p^0, Pa) and temperatures for each gas mixture using the ideal gas law,

$$\rho_g^0 = \frac{p^0 W_g}{R_{ig} T_g^0}. \tag{40}$$

Where W_g is the molecular weight (kg mol^{-1}) of the gas mixture. The initial gas velocities (u_g^0, m s^{-1}) were obtained from the inlet mass flow rates ($\dot{m}_g^0$, kg s^{-1}), densities, and channel cross sectional area according to

$$u_g^0 = \frac{\dot{m}_g^0}{\rho_g^0 w_{ch} h_{ch}}. \tag{41}$$

Where w_{ch} and h_{ch} are the width and depth of a single channel. The mass flow rates of the gas inlet were determined from the stoichiometric relationships of the charge-transfer reactions (Eqs. (1) and (2)) and therefore depend on the applied current density (j_{appl}, A m^{-2}). In the fuel channel, the reactant mass flow rate ($\dot{m}_k^0$, kg s^{-1}) is

$$\dot{m}_k^0 = \frac{|\nu_k| j_{appl} L_{ch} w_{act} W_k}{nF U_{F,k}}, \tag{42}$$

where ν_k is the stoichiometric coefficient of species k (dimensionless), L_{ch} is the channel length (m), w_{act} is the width of the active area below the channel (m), n is the number of electron transfer (dimensionless), F is the Faraday constant (96 485 C mol^{-1}) and $U_{F,k}$ is the fuel utilisation factor (dimensionless) for reactant species k. The inlet fuel mass flow rate ($\dot{m}_{fuel}^0$, kg s^{-1}) follows from

$$\dot{m}_{fuel}^0 = \dot{m}_k^0 / Y_k^0, \tag{43}$$

where Y_k^0 is the inlet mass fraction of species k. The reactant species k was selected based on the operating mode: hydrogen for SOFC mode and steam for SOEC mode. For the air channel, the inlet flow rate ($\dot{m}_{air}^0$, kg s^{-1}) is

$$\dot{m}_{air}^0 = \varepsilon_{air} \frac{|\nu_{O_2}| j_{appl} L_{ch} w_{act} W_{air}}{nF X_{O_2}^0}, \tag{44}$$

where ε_{air} is the excess air ratio (dimensionless) and $X_{O_2}^0$ is the molar fraction of oxygen in air (dimensionless). These expressions ensure that the inlet mass flow rates remain consistent with the instantaneous electrochemical load.

All models of the rSOC stack and the Balance of Plant components were implemented as individual MATLAB functions and assembled in SIMULINK as separate subsystems to preserve a modular structure. Each function was standardised to receive an input vector containing temperature, pressure, mass flow rate, and gas composition. Once this interface was defined, all subsystems were connected according to the process flow diagram in Fig. 1. To obtain a consistent initial condition for the complete plant model, the rSOC stack model was first integrated over 10 s using a relaxed absolute tolerance of the order of ten and a relative tolerance of 10^{-6}. This preliminary run allowed the solver to converge even when the initial state was far from equilibrium. The resulting steady state profiles of temperature, pressure, mass flow rate, and gas composition were stored and used as initial conditions for the main dynamic simulation, which employed stricter tolerances of 10^{-6} for both absolute and relative values.

For all dynamic BoP units, steady state conditions were obtained iteratively using the MATLAB solver `fsolve`. In the air circuit, the initialisation started with Heat Exchanger 2, whose outlet conditions were used as inputs for Heater 3. The process was repeated sequentially until steady operation was reached in both components. In the fuel circuit, the hydrogen tank was initialised independently using its design operating pressure, temperature, and total mass. Its outlet flow passed through a control valve that determined the pressure and temperature of the pure hydrogen stream. These were then used to initialise Heater 1. For the evaporator, the outlet temperature of the condenser was fixed at 313.15 K, which defined the inlet condition of stream 20 entering the water balance point. The inlet water temperature (stream 22) was set to 298.15 K in SOEC mode, whereas in SOFC mode outlet water (stream 21) left the system at 315.15 K. With these boundary conditions, the pump increased the pressure to establish the inlet state of stream 2 and the evaporator was simulated until steady state was reached. Once the conditions of streams 3 and 6 were known, they were combined in the mixer to form stream 7, which entered Heat Exchanger 1. The hot stream 10 entering Heat Exchanger 1 corresponded to the outlet conditions of the stack, previously obtained from the 10-second dynamic simulation. This allowed the steady state of Heat Exchanger 1 to be computed and then used to initialise Heater 2.

The integrated system was first evaluated under a reference condition, considering a gas inlet temperature of 750 °C, an air excess ratio of 8, a fuel utilisation of 0.55 and a hydrogen molar fraction of 0.5. The inlet pressure of the stack was fixed at one atmosphere.

The complete dynamic simulation was then performed in SIMULINK over a twenty four hour period. The applied current density varied dynamically according to either the electrical demand or the hydrogen production requirement. Within the rSOC subsystem, the required inlet mass flow rates were computed internally as functions of the instantaneous current density using Eqs. (42) to (44). The fuel utilisation factor, excess air ratio, and inlet hydrogen molar fraction were kept constant. The resulting mass flow rates were passed as instantaneous control signals to the air blower, the hydrogen tank valve, and the water pump, which adjusted the inlet conditions supplied to the rSOC stack.

To assess the practical applicability of the developed model, computational costs were evaluated. Simulating a 0.1 s transient period for the isolated stack requires approximately 3 s of computation time. For the fully integrated plant, the complete 24-hour solar-driven duty cycle is simulated in approximately 2 minutes. These runtimes were achieved using a single core of an 11th Gen Intel Core i7-11700 processor at 4.5 GHz.

4. Case study

The case study considers the operation of an rSOC plant coupled with real solar generation data obtained from the Diego de Almagro Photovoltaic Park, located in the Atacama Region of Chile, one of the areas with the highest solar radiation in the world [51]. The high availability of solar resources in this region makes it an ideal place to evaluate the integration of energy conversion and storage technologies that operate flexibly according to supply and demand. Fig. 2 shows the daily solar generation curve scaled to 0.25% of the total installed capacity of the photovoltaic park, alongside the electricity demand profile of 250 residential apartments. The scaling factor was defined based on the maximum power consumption of the rSOC plant in SOEC mode, equivalent to 499.8 kW, while the demand in SOFC mode was determined from the average daily consumption of 250 apartments, corresponding to a peak of 223.4 kW.

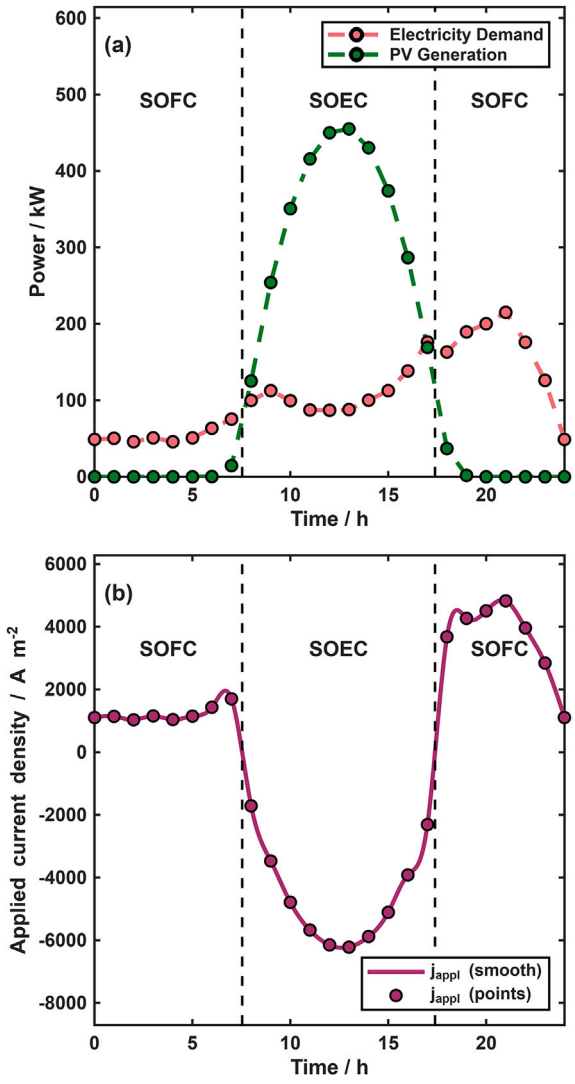


Fig. 2. Comparison between the solar generation profile and the electricity demand curve used to define the reversible operation of the rSOC system. 24-hour cycle to define the operation of the rSOC plant. (a) Scaled photovoltaic power generation (SOEC mode) and residential electricity demand (SOFC mode); and (b) Derived applied current density, including the transition between both operating modes.

The solar generation data were obtained from the Chilean Ministry of Energy's Solar Exploration Platform [52], which provides hourly solar generation profiles. The residential demand profile was adapted from the work of [53], which reports aggregated hourly electricity consumption patterns for multiple households. The available data provide hourly averages over a 24-hour period rather than complete time series. From these hourly points, the applied current density was derived based on the photovoltaic generation during SOEC mode and the electricity demand during SOFC mode. The resulting discrete j_{appl} values were smoothed into a continuous curve, which was then used as the input current profile in the SIMULINK dynamic model. The vertical dashed black lines in Fig. 2 indicate the rSOC plant's operating modes: SOEC (08:00–18:00), when excess solar energy is used to produce hydrogen, and SOFC (00:00–08:00 and 18:00–00:00), when electricity is generated from stored hydrogen to meet residential demand. This integrated representation enables a clear visualisation of the complementarity between renewable energy availability and plant operation in both modes.

5. Results and discussion

5.1. Validation of the rSOC stack model

5.1.1. Polarisation curve

Experimental polarisation data of a 4×4 cm^2 active area SOC supported by the fuel electrode were used to validate the model [54]. The cell comprises a thick Ni/YSZ cermet fuel electrode, a YSZ electrolyte, and a thinner LSM/YSZ composite air electrode. Operation in SOEC and SOFC modes was tested using pure oxygen at the air electrode and a fuel mixture of 50% H_2O and 50% H_2 at the fuel electrode, considering two temperatures, 750 °C and 850 °C. Geometric parameters and material properties for this experimental setup are reported in [24]. Simulations were performed using the calibrated kinetic parameters reported by Wang et al. [28], which are listed in Table A.2. It is worth noting that no additional parameter calibration was performed. Fig. 3 compares the simulated cell polarisation with the experimental data from [54]. The model was able to reproduce the experimental polarisation curve at both 750 °C and 850 °C, yielding mean absolute percentage errors (MAPE) of 2.01% and 1.95%, respectively.

5.1.2. Time constants

Since the insulated rSOC stack was modelled as a single representative repeating unit (including PEN, channels and interconnect), it is critical to verify that the dynamic thermal and electric response remains physically consistent. The dynamic response during mode switching (from SOEC to SOFC) was validated against simulation results reported by Wehrle et al. [24] for the stack's average solid temperature and current density following an imposed voltage step from approximately 1.2 V down to 0.7 V. In this study, we applied a current-density step rather than a voltage step, as this better aligns with the model's configuration. The current density was stepped from -4.5 A m^{-2} (SOEC mode) to 9.4 A m^{-2} (SOFC mode), which is equivalent to the voltage change reported by Wehrle et al. [24].

Fig. 4 presents the deviation in average stack temperature and cell voltage profiles (i.e., the difference between the current value of the process variable and its nominal steady-state value before the step change) for the imposed step change in current density. The time axis was shifted so that the step occurs at $t = 0$. Following the perturbation, the stack temperature and cell voltage exhibit distinct transient behaviours as shown in (Table 3, Eqs. (45) and (46), respectively). The average stack temperature ($T_{stack,avg}$, °C) was fitted with a first-order (FO) model, yielding an

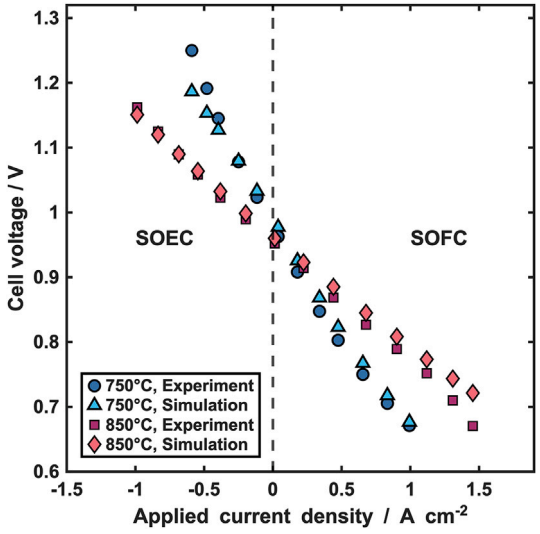


Fig. 3. Comparison of polarisation curves between simulation results and experimental data reported by Ebbesen et al. [54] at a temperature of 1023.15 K and 1123.15 K with fuel at 50% H_2O/50% H_2 and pure oxygen.

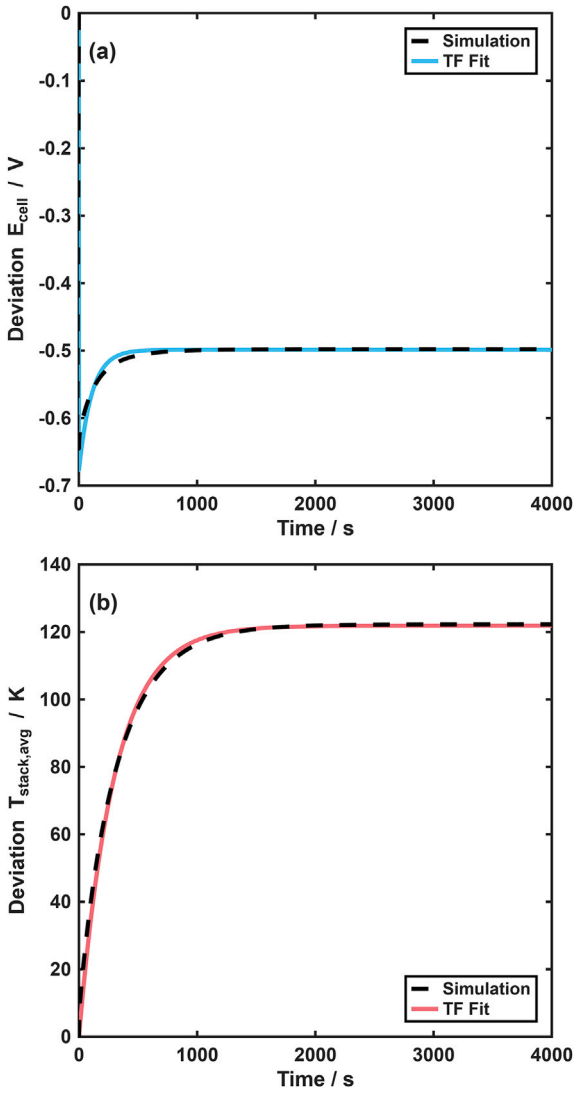


Fig. 4. Dynamic response of the isolated stack to an imposed current density step from −4.5 A m^{-2} to 9.4 A m^{-2}, at T_g^{in} = 1023.15 K, and a fuel feed composition of 50% H_2O / 50% H_2 and pure oxygen. (a) Deviation in cell voltage and transfer-function fit; (b) Deviation in average stack temperature and transfer-function fit.

average time constant of $\tau \sim 299$ s with a gain $K \sim 9 \times 10^{-3}$ K m^2 A^{-1}. The cell voltage (E_{cell}, V) was represented using two parallel FO elements. The first transfer function is characterised by $\tau_1 \sim 2 \times 10^{-2}$ s and $K_1 \sim$-5 $\times 10^{-5}$ V m^2 A^{-1}, while the second transfer function is defined by $\tau_2 \sim 108$ s and $K_2 \sim 1 \times 10^{-5}$ V m^2 A^{-1}. The slower evolution of the thermal response is expected, since heat transfer processes such as thermal energy accumulation and dissipation within the solid structure operate on longer timescales. The shorter electrical time constant reflects the direct dependence of the electrochemical reactions on the applied current, whereas the longer thermal time constant arises from the slower response of the solid materials.

To allow for comparison of gains, the simulation results of [24] were analysed to extract analogous gains with respect to current density. No specific transfer function fittings were presented to characterise the stack deviation responses in their study. A gain of ~0.0158 K m^2 A^{-1} and ~1 × 10^{-5} V m^2 A^{-1} was obtained for the average stack temperature and voltage, respectively. These gains are similar in magnitude to the thermal and electrochemical process gains resulting from our model.

They also reported that the electrical response adjusts considerably faster than the thermal response, with characteristic times of approximately $\tau \sim 100$ s and $\tau \sim 339$ s, respectively. These time constants are of the same order of magnitude as those obtained in this work. Wehrle et al. [24] further reported that the thermal response is 3.4 times slower than the electrical one. A similar trend is observed here, with the thermal response being 2.8 times slower than the electrical response. Wehrle et al. [24] employ a hierarchical multi-scale framework that combines molecular-scale processes with three-dimensional representations of planar cells and stacks. In contrast, the present work adopts a simplified one-dimensional stack model. This reduced spatial resolution likely explains the smaller thermal time constant obtained here, as higher-dimensional models capture additional sources of thermal inertia that may not be fully represented in a one-dimensional formulation.

5.2. Verification of BoP unit models

A verification of all dynamic BoP components was performed before coupling them to the rSOC stack model to simulate the plant dynamics. The hydrogen storage tank, the three electric heaters, the two plate heat exchangers and the water evaporator were evaluated independently to confirm that each unit exhibits the correct dynamic and thermal response under representative operating conditions. The simulations validated key behaviours, including the charge–discharge thermodynamics of the hydrogen tank, the dependence of heating time on inlet mass flow rate and temperature in the electric heaters, the transient wall–fluid interactions and thermal delays in the heat exchangers, and the phase-change dynamics of the evaporator. All supporting figures and transient profiles are reported in the Supplementary Information (SI).

5.3. Dynamic coupling of the 1-D SOC model with the BoP models

As noted in Section 3.3, the integrated plant model, including the rSOC stack and BoP units, requires a consistent initial condition. This

Table 3
Transfer function models used to fit the dynamic responses for the isolated stack and for the integrated rSOC plant.

Variable	Transfer function	Model	Eq.
Isolated rSOC stack			
$T_{stack,avg}$ / K	FO (single 1st-order)	$G(s) = \frac{K}{\tau s + 1}$	(45)
E_{cell} / V	Parallel FOs (two 1st-order lags in parallel)	$G(s) = \frac{K_1}{\tau_1 s + 1} + \frac{K_2}{\tau_2 s + 1}$	(46)
Coupled rSOC plant			
$T_{stack,avg}$ / K	Parallel 1st-order lag + 2nd-order	$G(s) = \frac{K_1}{\tau_1 s + 1} + \frac{K_2}{\tau_2^2 s^2 + 2\zeta\tau_2 s + 1}$	(47)
E_{cell} / V	Parallel two 1st-order lags + 2nd-order	$G(s) = \frac{K_1}{\tau_1 s + 1} + \frac{K_2}{\tau_2 s + 1} + \frac{K_3}{\tau_3^2 s^2 + 2\zeta\tau_3 s + 1}$	(48)

condition was computed using the initial value of the current density (j_{appl} = 1102.88 A m^{-2}) as shown in Fig. 2. The resulting steady state properties of all process streams are listed in the Supplementary Information. Using this initial condition, a 24-hour cycle was simulated to track thermal and electrical stack responses, using the following control variables, X_{H_2} = 0.50, U_F = 0.55, X_{O_2} = 0.21, ε_{air} = 8, and T_g^{in} = 1023.15 K. To provide a realistic operating scenario, the air electrode used a simplified air binary mixture, containing 21% oxygen and 79% nitrogen instead of pure oxygen. This mixture was also used in the following subsections. Stack performance was assessed through its electrical efficiency based on the lower heating value (LHV), defined as

$$\eta_{el,stack}^{SOFC} = \frac{P_{stack}}{\dot{m}_{H_2} LHV}, \qquad \eta_{el,stack}^{SOEC} = \frac{\dot{m}_{H_2} LHV}{P_{stack}}, \tag{49}$$

for SOFC and SOEC modes, respectively. The stack thermal stress was represented by the maximum pseudo 2-D temperature gradient, defined as

$$|\nabla T|_{max} = \max\left(\sqrt{\left(\frac{dT_s}{dy}\right)^2 + \left(\frac{dT_s}{dz}\right)^2}\right), \tag{50}$$

which was calculated considering the temperature of the solid domains (T_s, K). This is a critical control variable in solid oxide stacks and should ideally remain below 10 K cm^{-1} to limit thermal stress-induced strain which can lead to degradation or failure [55]. Fig. 5 presents the dynamic profiles of the main stack variables, namely the power output, the outlet channel gas temperatures ($T_{f,out}$ and $T_{a,out}$, K, for the fuel and air sides, respectively), the average solid temperature ($T_{stack,avg}$, K), the maximum temperature gradient within the solid domains ($|\nabla T|_{max}$, K cm^{-1}) and the electrical efficiency ($\eta_{el,stack}$, dimensionless).

During both operating modes, the stack power closely follows the imposed current profile, delivering electricity during SOFC mode and consuming power during SOEC mode for hydrogen production, as shown in Fig. 5(a). The higher power delivered or consumed by the stack during simulation arises due to the calculation of the applied current density, assuming a constant nominal cell voltage. The simulated cell voltage varies dynamically and is generally higher than the assumed nominal values. Smooth transitions at mode switching indicate the effective thermal management of the stack. As mode transitions were simulated using a continuous current density profile, a localised reduction in efficiency is observed in Fig. 5 near the switching point. This did not produce instability in the balance-of-plant units owing to their thermal inertia. The thermal control is achieved through the electric heaters that activate when the target inlet gas temperature of 750 °C is not reached at the outlet gas in the heat exchangers (Fig. 1). The outlet gas temperatures and the average solid temperature of the stack (Fig. 5b) follow the electrical load, increasing in SOFC mode and decreasing during SOEC mode. This behaviour reflects the exothermic nature of SOFC operation and the heat sink required to drive electrolysis when operating below the thermo-neutral point in SOEC mode. This heat is taken from the hot gaseous streams entering the stack. The thermal response exhibits a noticeable lag compared to power changes, demonstrating the influence of BoP thermal inertia, which is discussed in detail in Section 5.5.

During SOFC operation, the electrical efficiency of the stack varies around 40% (Fig. 5d). Periods with higher current density result in lower electrical efficiencies and a larger $|\nabla T|_{max}$ (Fig. 5c). This reflects the increase in electrochemical reaction rates and ohmic heat generation under high load conditions. Immediately after switching from SOFC to SOEC, the stack displays a steep temperature drop; however, as the current continues to increase (Fig. 5b), the temperature and $|\nabla T|_{max}$ level off, indicating that cell voltage has approached or slightly exceeds the thermo-neutral voltage. This is reflected in the electrical efficiency (Fig. 5d), which initially exceeds one—for endothermic operation where part of the energy required for electrolysis is supplied as heat—and later drops below one corresponding to the transition to slightly exothermic behaviour. These coupled thermal and electrical trends highlight the importance of predictive control strategies to ensure stable operation under reversible operation. The maximum gradient in the solid stack temperature (Fig. 5d) was for the most part higher than 10 K cm^{-1} for the reference values of control variables used, displaying higher relative values with respect to the absolute applied current density in SOFC than in SOEC. Therefore, optimising control variables—such as fuel utilisation, air excess ratio, and inlet gas temperature—can effectively reduce thermal gradients and improve electrical efficiency.

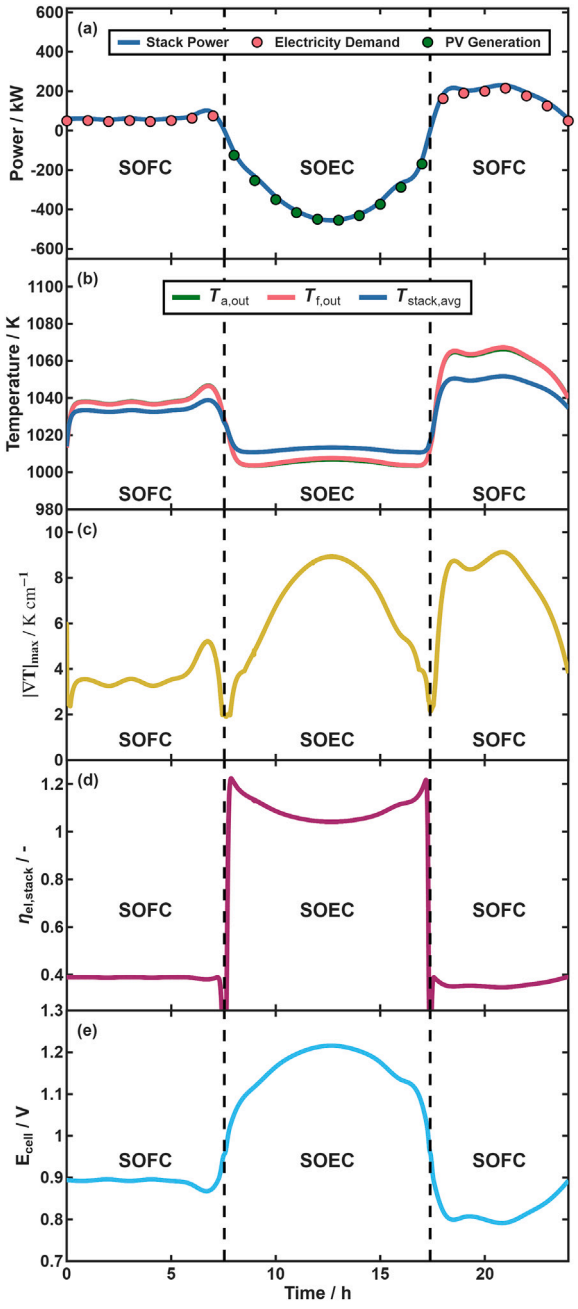


Fig. 5. Operating profile of the rSOC plant over a 24-hour cycle including (a) the imposed solar-derived power demand; (b) the thermal response of the air and fuel outlets and the average stack temperature; (c) the maximum solid temperature gradient within the stack; (d) the electrical efficiency of the stack, and (e) the cell voltage. The four control variables remain constant throughout the cycle with values X_{H_2} = 0.50, U_F = 0.55, ε_{air} = 8, and T_g^{in} = 1023.15 K.

Table 4
Range values for the four factors considered in the LHS design.

Control factor[a]	Symbol	Range	Unit
Inlet gas temperature	T_g^{in}	973.15 – 1073.15	K
		700 – 800	°C
Inlet H_2 molar fraction	$X_{H_2}^{in}$	0.5 – 0.9	–
Air excess ratio	ϵ_{air}	4 – 12	–
Fuel utilisation factor	U_F	0.2 – 0.9	–

[a] Air inlet composition fixed at 21%O_2/79%N_2

5.4. Experimental design and multi-objective optimisation

An experimental design was developed to demonstrate that an optimal operating point can be identified that maximises the electrical efficiency of the stack while minimising the temperature gradients within the solid domains. LHS was employed to maximise information coverage across the input space with minimal simulations, in line with standard practice for complex codes [56]. A design matrix of 18 computational experiments was created to explore two responses, stack electrical efficiency and maximum temperature gradients, as a function of four variables: air excess ratio, fuel utilisation factor, hydrogen molar fraction, and gas temperature at the stack inlet. This sample size was sufficient given the resulting high R^2 (> 0.94) and significant p-values in the surrogate models.

The analysis was conducted for the SOFC mode, which is used as a representative case, although the same methodology can be applied to SOEC operation. The study was carried out at an applied current density of j_{appl} = 4829.07 A m^{-2}, which corresponds to the operating condition associated with the highest thermal gradient of 9.2 K cm^{-1} and the lowest efficiency of 0.34 when excluding transition points between operating modes (Fig. 5(c) and (d)). A Latin Hypercube Sampling (LHS) strategy was adopted to ensure a uniform coverage of the ranges of four factors. These factors included the four control variables described before, inlet gas temperature, inlet hydrogen molar fraction, air excess ratio, and fuel utilisation. Table 4 summarises the range values for each factor. A total of eighteen dynamic simulations were carried out, which corresponded approximately to the resolution of a fractional Central Composite Design. The eighteen sampled cases are provided in Supplementary Information.

The results of these simulations were used to construct surrogate models through response surface methodology (RSM) for both objectives, the electrical efficiency ($\eta_{el,stack}$) and the maximum temperature gradient in the solid domains ($|\nabla T|_{max}$). Polynomial regression, including linear, quadratic and interaction terms, was applied after normalising all variables. Terms that were not statistically significant as indicated by a p-value lower than 0.05 were removed one by one. Table 5 summarises the final regression coefficients, t-statistics and p-values obtained from the fitted response surfaces. Both models achieved high coefficients of determination ($R^2 > 0.94$), confirming that they adequately represented the simulation results.

Table 5
Estimated regression coefficients, t-statistics, and p-values for electric efficiency and maximum gradient of solid temperature of the stack.

Variable	Coefficient	t	p-value
Electric efficiency ($\eta_{el,stack}$), $R^2 = 1$			
Constant	0.3555	322.93	0.000
U_F	0.1272	150.45	0.000
$X_{H_2}^{in}$	0.0054	6.3963	0.000
T_g^{in}	0.0054	6.9583	0.000
U_F^2	−0.0020	−2.3198	0.037
Maximum temperature gradient ($\|\nabla T\|_{max}$), $R^2 = 0.947$			
Constant	9.4771	68.191	0.000
ϵ_{air}	−1.3463	−13.854	0.000
U_F	0.3486	3.4903	0.004
T_g^{in}	−0.3732	−3.7630	0.002
ϵ_{air}^2	0.3347	3.0811	0.008

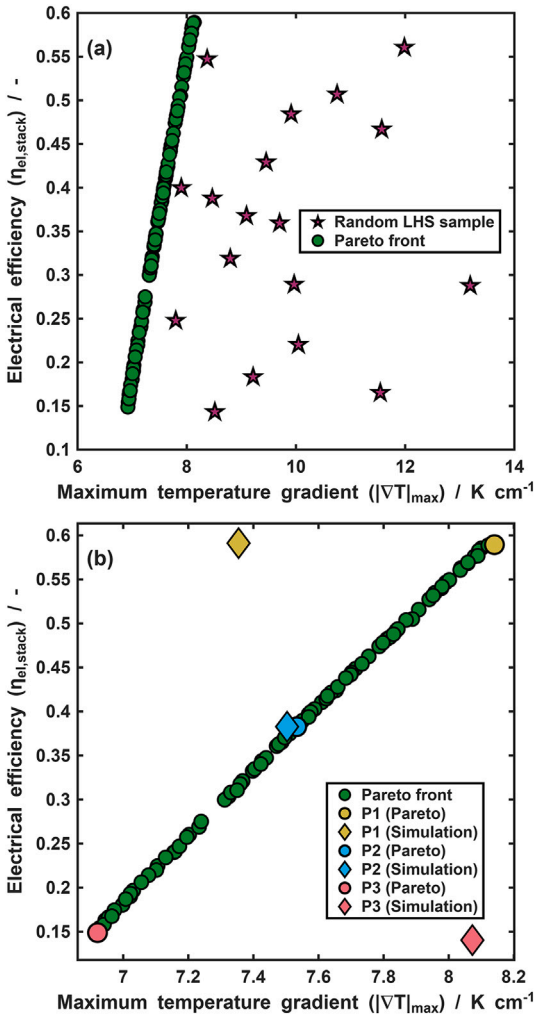


Fig. 6. Multi-objective optimisation results for SOFC mode. (a) Pareto front showing the trade-off between stack electrical efficiency and the maximum temperature gradient, together with LHS samples; (b) Magnified view of the optimal region, including the Pareto front and selected points used for model validation.

The optimisation was performed using the `gamultiobj` algorithm from the MATLAB Global Optimisation Toolbox. This method applies a genetic algorithm that approximates the Pareto-optimal front. The obtained Pareto front for SOFC operation is shown in Fig. 6, where the trade-off between stack efficiency and thermal gradient is clearly observed. The optimal region corresponds to the solutions where the efficiency increases without inducing excessive thermal stress, defining a practical operating window for the system operating in SOFC mode at the tested current density.

In Fig. 6(a), the green circles depict the Pareto-optimal solutions obtained from the response surface optimisation, outlining the expected trade-off between stack electrical efficiency and maximum thermal gradient. The purple stars correspond to the dynamic simulation results of the initial design points sampled across the input space. A detailed view of the optimal region is presented in Fig. 6(b), highlighting three selected operating conditions (P1–P3) marked by diamonds, along with their corresponding dynamic simulation outputs shown as circles. The specific control settings for these cases are summarised in Table 6 and include ϵ_{air} from 11.82 to 12, U_F from 0.20 to 0.90, $X_{H_2}^{in}$ from 0.84 to 0.89, and $T_g^{in} \sim 1073$ K.

Table 6
Comparison of performance and optimised control settings for selected Pareto points, including simulation results from the integrated rSOC plant model (Fig. 6b).

Case	$\eta_{el,stack}$ / –		$\lvert\nabla T\rvert_{max}$ / K cm^{-1}		Control variables[a]			
	Pareto	Simulation	Pareto	Simulation	ε_{air}	U_F	$X^{in}_{H_2}$	T^{in}_g / K
P1	0.589	0.590	8.129	7.344	11.82	0.90	0.89	1072.88
P2	0.379	0.379	7.523	7.509	12	0.55	0.86	1072.93
P3	0.150	0.140	6.914	8.022	12	0.20	0.84	1073.03

[a] Air inlet composition fixed at 21%O_2/79%N_2

Compared to the baseline solar-driven configuration, the optimised operating strategies achieved significant performance improvements. The maximum solid temperature gradient, $|\nabla T|_{max}$, was reduced from 9.2 K cm^{-1} to 7.34 K cm^{-1}, corresponding to an average reduction of 20%. At the same time, the stack electrical efficiency, $\eta_{el,stack}$, increased from 0.34 to 0.59, representing an average improvement of 73.5%. Full simulation results are reported in Table 6. The relative prediction errors were below 0.2% for both electric efficiency and maximum temperature gradient at P2, indicating good agreement between the model and optimisation results. For P1, the errors were 0.24% in efficiency and 9.7% in temperature gradient, while for P3 they reached 6.7% and 16%, respectively. These results suggest that the model is highly accurate around P2, with reduced accuracy at P1 and P3. Notably, P1 yields a solution that slightly outperforms the Pareto front, achieving both higher efficiency and a lower temperature gradient. The larger error in the temperature gradient is a direct result of the lower fitting R^2, indicating a highly non-linear response. Nevertheless, the optimisation successfully identifies operating conditions that simultaneously maximise stack efficiency and reduce thermal gradients, with an error of less than 1 K cm^{-1}.

5.5. Dynamic response analysis of the coupled rSOC system

The yellow Pareto point in Fig. 6(b) (P1) was selected to evaluate the dynamic behaviour of the integrated system under representative operating conditions. This point corresponds to an inlet gas temperature of 1072.88 K, an inlet hydrogen molar fraction of 0.89, an air excess ratio of 11.82, and a fuel utilisation factor of 0.9.

The SIMULINK model was first simulated for 3000 s to reach steady state at the maximum current density in SOFC mode, 4829.07 A m^{-2} in Fig. 2(b). A step change of 10% was then applied, increasing the current density to 5311.98 A m^{-2}. The step was smoothed using a hyperbolic tangent function, and the deviation variables were plotted so that the transient responses begin at zero (Fig. 7). The system was simulated until the new steady state was reached.

The dynamic responses shown in Fig. 7 exhibit the characteristic overshoot, undershoot and damped behaviour typically observed in integrated SOC systems where the stack interacts with BoP units. For example, Liu et al. [31] reported stack temperature transients with noticeable overshoot, undershoot and stabilisation times of several thousand seconds in a dynamic rSOC system including heat exchangers. Likewise, Yin et al. [34] observed comparable overshoot and undershoot behaviour and damped responses in inlet gas temperatures in a dynamically modelled SOEC-based power-to-gas system. The consistency of these transient trends supports the physical plausibility of the plant-level dynamics predicted by the present model.

Two parallel transfer function elements were required to model the coupled dynamic response of the average stack temperature, as shown in Eq. (47). The initial undershoot was described by a first-order term with $\tau_1 \sim 88$ s and $K_1 \sim$-0.06 K m^2 A^{-1}. The latter overshoot was captured by a second-order term with $\tau_2 \sim 208$ s and $K_2 \sim 0.07$ K m^2 A^{-1} with a damping factor $\zeta \sim 0.76$. This inverse and underdamped behaviour reflects the additional thermal inertia and dynamic coupling introduced by the auxiliary units.

Table 3 shows that three parallel transfer functions were required to model the coupled dynamic response of the cell voltage (Eq. 48). The

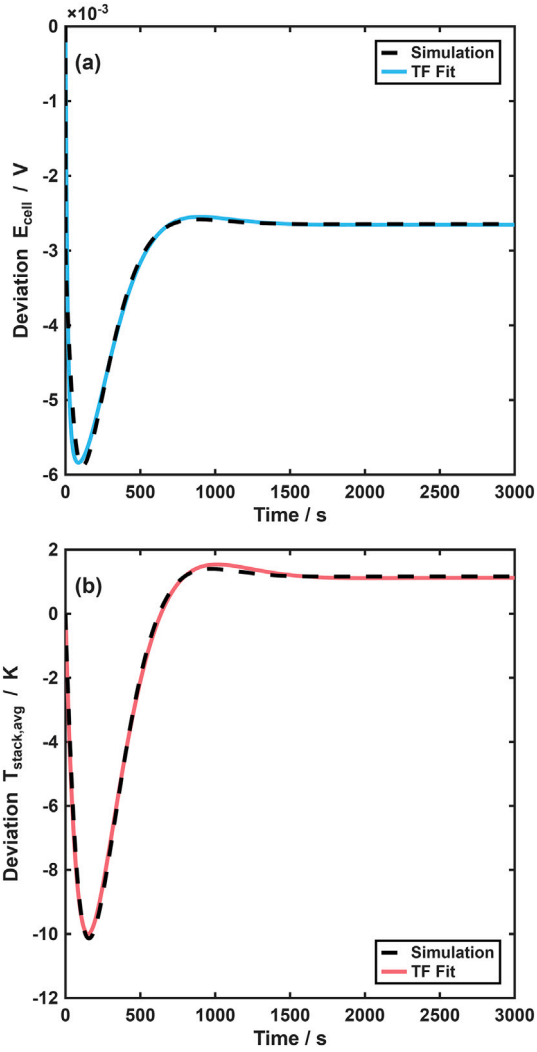


Fig. 7. Dynamic response of the coupled rSOC system at the operating point selected from the Pareto-front midpoint. A 10% increase in current density is applied. (a) Corrected cell voltage and transfer-function fit. (b) Corrected average stack temperature and transfer-function fit.

first term was an FO contribution with $\tau \sim 13$ s and a negative gain $K \sim$-1 × 10^{-6} V m^2 A^{-1}. The second term was an FO with $\tau \sim 211$ s and $K \sim$-6 × 10^{-7} V m^2 A^{-1}. The third term was a second-order transfer function with $\tau \sim 179$ s, $K \sim 1.1 \times 10^{-6}$ V m^2 A^{-1} and a damping factor $\zeta \sim 0.81$.

Analysis of the second-order terms shows that, for the cell voltage, the real parts of its poles yield an effective slow time scale of approximately $\tau^{eff} \sim 219$ s, whereas the thermal dynamics evolve over a comparable slow time scale of $\tau^{eff} \sim 273$ s. In the isolated stack (Section 5.1.2), the average stack temperature responds 2.8 times slower than the cell voltage, indicating a clear separation between the thermal

and electrochemical dynamics. In the integrated system, this ratio decreases to about 1.25, revealing that both subsystems now evolve over much more similar time scales. This reduction occurs because the stand-alone electrical dynamics do not show the oscillatory behaviour characteristic of the thermal subsystem; once the auxiliary units are coupled, the underdamped thermal mode introduces additional inertia and oscillatory features that propagate into the electrical response. As a result, voltage and temperature exhibit comparable dynamic behaviour, reflecting the strong coupling introduced by the integrated plant.

5.6. Rules of thumb for system design and operation

To bridge the gap between the detailed numerical analysis and practical engineering applications, several qualitative guidelines and trend-based rules-of-thumb can be extracted from the dynamic simulations and optimisation results. First, the integrated plant reveals that balance-of-plant thermal inertia heavily couples the electrical and thermal domains. Consequently, controllers must be tuned to the slower, underdamped thermal time scales ($\tau \sim 300$ s) rather than the inherently fast electrochemical timescales to avoid closed-loop instability during load variations. Second, thermal and electrical management are sensitive to independent process variables. The multi-objective optimisation demonstrates that the air excess ratio (ε_{air}) acts as the primary lever for thermal management by reducing spatial temperature gradients, whereas fuel utilisation (U_{F}) is the dominant driver for electrical efficiency. An optimal operating strategy safely maximises performance by employing high air excess ratios alongside high fuel utilisation. Finally, during mode switching between SOFC and SOEC operations, sharp thermal transients occur. It is critical that operational strategies maintain baseline reactant mass flows even when the applied current crosses zero to prevent flow starvation at the auxiliary units.

6. Conclusions

Previous research on rSOC has primarily focused on the stack in isolation, using zero- to three-dimensional simulations under steady-state and dynamic conditions to investigate electrochemical performance and thermal behaviour. A notable weakness in these studies has been the absence of dynamic BoP effects, neglecting inertia and transient interactions of auxiliary components, which in turn led to an overestimation of the operational plant flexibility. This study developed a comprehensive dynamic rSOC plant model coupling a one-dimensional dynamic rSOC stack model with dynamic BoP components. The model implemented in MATLAB/Simulink enabled integrated simulation of both SOFC and SOEC modes under changing operating conditions.

Dynamic simulations revealed that BoP thermal inertia significantly slows down the system's response and introduces oscillatory behaviour, resulting in stack average temperature and cell voltage responding on similar timescales due to strong thermal–electrical coupling. Considering this realistic behaviour, a multi-objective optimisation successfully identified an optimal operating point for the rSOC plant for a representative SOFC mode leading to both an increase in stack electrical efficiency and a reduction in the maximum stack temperature gradient relative to nominal settings, mitigating thermal stress and enhancing performance. This work bridges the gap between detailed stack models and full plant simulations, thereby providing a realistic tool for evaluating rSOC performance in renewable-integrated power systems. One key contribution is the determination of consistent time constants for both the cell voltage and the average stack temperature, which characterise the coupled and non-monotonic dynamic behaviour of the integrated plant. This highlights the importance of considering both the difference between the thermal and electrical time scales and the presence of inverse response when assessing the operational flexibility and transient stability.

The study's novelty lies in demonstrating that the aforementioned complex dynamic features emerge when the BoP dynamics are fully modelled alongside the stack, thereby revealing behaviours that remain hidden in isolated or steady-state representations. This improved characterisation offers practical insights for operational planning, real-time energy management, and the development of control strategies that must accommodate the intrinsic dynamic coupling of the plant. The locally identified transfer functions are valid only in the vicinity of the analysed operating point, and the highly non-linear nature of the real rSOC plant may change the magnitude or sign of the inverse response under different conditions. This introduces practical constraints for controller tuning and may lead to unstable closed-loop behaviour if not properly addressed. Future research is recommended to focus on advanced control strategies, such as Internal Model Control (IMC), which are specifically suited to handling nonlinear dynamics with inverse response and can provide robust closed-loop performance under renewable-driven variability.

CRediT authorship contribution statement

Maite Arce-Reyes: Writing – review & editing, Writing – original draft, Visualisation, Validation, Software, Methodology, Investigation, Formal analysis, Data curation. **Felipe Huerta:** Writing – review & editing, Supervision, Software, Methodology, Formal analysis, Validation. **Simón Díaz-Quezada:** Writing – review & editing, Software, Methodology, Formal analysis. **José R. Pérez-Correa:** Writing – review & editing, Writing – original draft, Supervision, Software, Methodology, Formal analysis. **Nigel P. Brandon:** Writing – review & editing, Funding acquisition, Formal analysis. **Catalina A. Pino-Muñoz:** Writing – review & editing, Writing – original draft, Supervision, Software, Methodology, Formal analysis, Conceptualisation, Validation.

Declaration of competing interest

The authors declare that they have no known competing financial interests or personal relationships that could have appeared to influence the work reported in this paper.

Acknowledgements

C.A. Pino-Muñoz and N.P. Brandon acknowledge funding support from EPSRC (EP/W003597/1). M. Arce and F. Huerta appreciate the financial support from the project ANID FONDAP/1523A0006 'Solar Energy Research Centre' - SERC - Chile and the UC Energy Centre. We would like to thank Takahiro Machida for the insightful discussions regarding the rSOC model.

Appendix A. Model inputs and design parameters for the rSOC systems

Table A.1
Nominal operating parameters and number of rSOC stacks.

Parameter	Symbol	Unit	SOFC mode	SOEC mode
Current density (per electrode area)	j_{ed}	A cm^{-2}	0.683	−0.683
Stack temperature	T_{stack}	°C	750	750
Pressure	p	atm	1	1
Inlet molar composition (FE)	X_{H_2} / X_{H_2O}	–	90% / 10%	10% / 90%
Inlet molar composition (AE)	X_{O_2} / X_{N_2}	–	21% / 79%	21% / 79%
Equilibrium potential	E_{eq}	V		0.987
No. of cells, stacks, arrays and modules[a]				
No. of cells per stack	$N_{cells,stack}$	–		68
No. of stacks per array	$N_{stacks,array}$	–		10
No. of arrays per module	$N_{arrays,mod}$	–		10
No. of modules per plant	N_{mod}	–		1
Fuel electrode supported cell (FESC)				
Cell potential	E_{cell}	V	0.74	1.22
Power per stack	P_{stack}	kW	3.031	4.998
Power per module	P_{mod}	kW	303.158	499.801
Total power	P_{tot}	kW	303.158	499.801
Average power	P_{tot}^{avg}	kW		401.479

[a] Fixed values obtained considering FESC cell potentials and target plant power of 401.479 kW, taken as the average power between SOFC and SOEC power.

Table A.2
SOC stack design parameters and properties [28,36].

Parameter	Symbol	Value		Unit
		Ni/YSZ fuel electrode	LSM/YSZ air electrode	
Electrode kinetic parameters				
Pre-exponential factor	A_{ede}	3.5×10^6	1.56×10^5	A cm^{-2}
Activation energy	E_{ede}	102.4	104.5	kJ mol^{-1}
Charge transfer coefficient	β_{ede}	0.7	0.4	–
Geometric and thermal properties				
Stack/flow type	–	Planar/Co-flow		–
Interconnect/Frame material	–	Crofer 22 APU		–
Insulation material	–	Porous Promalight-1000X		–
Cell active area[a]	$A_{cell,act}$	88.208		cm^2
Cell length	L_{cell}	8		cm
RU width	w_{RU}	4.47		mm
Channel width	w_{ch}	2.98		mm
Channel length	L_{ch}	8		cm
Channel depth (height)	l_{ch}	1		mm
Interconnect rib width	$w_{int,rib}$	1.49		mm
Interconnect thickness	l_{frame}	0.75		mm
Frame thickness/width/lengths	l_{int}	0.01		m
Insulation thickness/width/lengths	l_{int}	0.05		m
Interconnect/Frame density	ρ_{int}	7700		kg m^{-3}
Insulation density	ρ_{ins}	280		kg m^{-3}
Interconnect/Frame specific heat capacity	$\hat{c}_{p,int}$	660		J kg^{-1} K^{-1}
Insulation specific heat capacity	$\hat{c}_{p,ins}$	1070		J kg^{-1} K^{-1}
Interconnect/Frame thermal conductivity	k_{int}	24		W m^{-1} K^{-1}
Insulation thermal conductivity	k_{ins}	0.0295		W m^{-1} K^{-1}
Interconnect/Frame emissivity	ϵ_{int}	0.6		–
Insulation emissivity	ϵ_{ins}	0.5		–
No of channels per cell width (RU)	N_{ch}	37		–

[a] Stack model implementation considers only the area under the channel as the active cell area.

Appendix B. Supplementary data

Supplementary data for this article can be found online at doi:10.1016/j.apenergy.2026.127974.

Data availability

Data will be made available on request.

References

[1] Calise F, Cappiello FL, Cimmino L, Vicidomini M, Dynamic simulation modelling of reversible solid oxide fuel cells for energy storage purpose, Energy 2022;260:124893, https://doi.org/10.1016/j.energy.2022.124893
[2] Mogensen MB, Chen M, Frandsen HL, Graves C, Hansen JB, Hansen KV, Hauch A, Jacobsen T, Jensen SH, Skafte TL, Sun X, Reversible solid-oxide cells for clean and sustainable energy, Clean Energy 2019;3(3):175–201. https://doi.org/10.1093/ce/zkz023

[3] Jiang SP, Challenges in the development of reversible solid oxide cell technologies: a mini review, Asia-Pac J Chem Eng 2016;11(3):386–91. https://doi.org/10.1002/apj.1987

[4] Venkataraman V, Pérez-Fortes M, Wang L, Hajimolana YS, Boigues-Muñoz C, Agostini A, McPhail SJ, Maréchal F, Van Herle J, Aravind PV. Reversible solid oxide systems for energy and chemical applications – review & perspectives. Technical report, 2019.

[5] Choudhury A, Chandra H, Arora A, Application of solid oxide fuel cell technology for power generation—a review, Renew Sustain Energy Rev 2013;20:430–42. ISSN 1364-0321, https://doi.org/10.1016/j.rser.2012.11.031, https://www.sciencedirect.com/science/article/pii/S1364032112006430.

[6] Mogensen MB, Chen M, Frandsen HL, Graves C, Hansen JB, Hansen KV, Hauch A, Jacobsen T, Jensen SH, Skafte TL, Sun X, Reversible solid-oxide cells for clean and sustainable energy, Clean Energy Oct 2019;3(3):175–201. ISSN 2515-4230, https://doi.org/10.1093/ce/zkz023

[7] Martsinchyk K, Martsinchyk A, Milewski J, Solid oxide electrolysis, Co-Electrolysis, and methanation fundamentals of performance and history, Energies Dec 2024;17:6486. https://doi.org/10.3390/en17246486

[8] Biswas S, Rathore SS, Kulkarni AP, Giddey S, Bhattacharya S, A theoretical study on reversible solid oxide cells as key enablers of cyclic conversion between electrical energy and fuel, Energies 2021;14(15). ISSN 1996-1073, https://doi.org/10.3390/en14154517

[9] Wang Y, Leung DYC, Xuan J, Wang H, A review on unitized regenerative fuel cell technologies, part-a: unitized regenerative proton exchange membrane fuel cells, Renew Sustain Energy Rev 2016;65:961–77. ISSN 1364-0321, https://doi.org/10.1016/j.rser.2016.07.046, https://www.sciencedirect.com/science/article/pii/S1364032116303628.

[10] Schwarze K, Posdziech O, Mermelstein J, Kroop S, Operational results of an 150/30 kw RSOC system in an industrial environment, Fuel Cells 2019;19:374–80. https://doi.org/10.1002/fuce.201800194

[11] Schwarze K, Geißler T, Nimtz M, Blumentritt R, Demonstration and scale-up of high-temperature electrolysis systems, Fuel Cells 2023;23:492–500. https://doi.org/10.1002/fuce.202300059

[12] Schiller G, Lang M, Szabo P, Monnerie N, von Storch H, Reinhold J, Sundarraj P, Solar heat integrated solid oxide steam electrolysis for highly efficient hydrogen production, J Power Sources 2019;416:72–8. https://doi.org/10.1016/j.jpowsour.2019.01.059

[13] Wang H, Zhang Q, Li X, Ma T, Sayfieva KF, Investigation into the hydrogen production performance of a novel 5-kw hybrid-system composed of a solar steam generator directly connected with conventional solid oxide electrolysis cells, Energy Convers Manag 2024;301:118023, https://doi.org/10.1016/j.enconman.2023.118023

[14] Baldinelli A, Barelli L, Bidini G, Cinti G, Michele AD, Mondi F, How to power the energy–water nexus: coupling desalination and hydrogen energy storage in Mini-Grids with reversible solid oxide cells, Processes 2020;8:1494. https://doi.org/10.3390/pr8111494

[15] Ghezel-Ayagh H. Reversible solid oxide fuel cell systems for energy storage and hydrogen production. Technical report, FuelCell Energy, Inc. Danbury, CT (United States), May 2022. https://www.osti.gov/biblio/1874500.

[16] Nuggehalli Sampathkumar S, Aubin P, Couturier K, Sun X, Sudireddy BR, Diethelm S, Pérez-Fortes M, Van herle J, Degradation study of a reversible solid oxide cell (rSOC) short stack using distribution of relaxation times (DRT) analysis, Int J Hydrog Energy 2022;47(18):10175–93. ISSN 0360-3199, https://doi.org/10.1016/j.ijhydene.2022.01.104, https://www.sciencedirect.com/science/article/pii/S0360319922001975.

[17] Wolf SE, Winterhalder FE, Vibhu V, de Haart LGJ (Bert), Guillon O, Eichel R-A, Menzler NH, Solid oxide electrolysis cells – current material development and industrial application, J Mater Chem A 2023;11:17977–8028. https://doi.org/10.1039/D3TA02161K

[18] Liu G, Wang Z, Liu X, Kupecki J, Zhao D, Jin B, Wang Z, Li X, Transient analysis and safety-oriented process optimisation during electrolysis–fuel cell transition of a novel reversible solid oxide cell system, J Clean Prod 2023;425:139000. ISSN 0959-6526, https://doi.org/10.1016/j.jclepro.2023.139000, https://www.sciencedirect.com/science/article/pii/S095965262303158X.

[19] Wehrle L, Wang Y, Boldrin P, Brandon NP, Deutschmann O, Banerjee A, Optimizing solid oxide fuel cell performance to re-evaluate its role in the mobility sector, ACS Environ Au 2022;2(1):42–64. https://doi.org/10.1021/acsenvironau.1c00014

[20] Banerjee A, Wang Y, Diercks J, Deutschmann O, Hierarchical modeling of solid oxide cells and stacks producing syngas via h_2o/CO_2 CO-electrolysis for industrial applications, Appl Energy 2018;230:996–1013. ISSN 0306-2619, https://doi.org/10.1016/j.apenergy.2018.08.122, https://www.sciencedirect.com/science/article/pii/S0306261918312960.

[21] Wendel CH, Gao Z, Barnett SA, Braun RJ, Modeling and experimental performance of an intermediate temperature reversible solid oxide cell for high-efficiency, distributed-scale electrical energy storage, J Power Sources 2015;283:329–42. ISSN 0378-7753, https://doi.org/10.1016/j.jpowsour.2015.02.113, https://www.sciencedirect.com/science/article/pii/S0378775315003596.

[22] Wendel CH, Braun RJ, Design and techno-economic analysis of high efficiency reversible solid oxide cell systems for distributed energy storage, Appl Energy 2016;172:118–31. ISSN 0306-2619, https://doi.org/10.1016/j.apenergy.2016.03.054, https://www.sciencedirect.com/science/article/pii/S0306261916303749.

[23] Kazempoor P, Braun RJ, Model validation and performance analysis of regenerative solid oxide cells: electrolytic operation, Int J Hydrog Energy 2014;39(6):2669–84. ISSN 0360-3199, https://doi.org/10.1016/j.ijhydene.2013.12.010, https://www.sciencedirect.com/science/article/pii/S036031991302908X.

[24] Wehrle L, Wang Y, Banerjee A, Brandon N, Deutschmann O, Dynamic modeling of reversible solid oxide cells, Chem-ing-tech Jun 2019;91(6):833–42. ISSN 0009-286X, https://doi.org/10.1002/cite.201800188. Publisher Copyright: ©2019 WILEY-VCH Verlag GmbH & Co. KGaA, Weinheim.

[25] del Pozo Gonzalez H, Torrell M, Bernadet L, Bianchi FD, Trilla L, Tarancón A, Domínguez-García JL, Mathematical modeling and thermal control of a 1.5 kw reversible solid oxide stack for 24/7 hydrogen plants, Mathematics 2023;11(2). ISSN 2227-7390, https://doi.org/10.3390/math11020366, https://www.mdpi.com/2227-7390/11/2/366.

[26] Wellen SG, Modelling study of the thermal management of a RSOC system [Master's thesis], University of Twente, Faculty of Engineering Technology - Mechanical Engineering, Apr 2024.

[27] Buffo G, Ferrero D, Santarelli M, Lanzini A, Energy and environmental analysis of a flexible Power-to-X plant based on reversible solid oxide cells (rSOCs) for an urban district, J Energy Storage 2020;29:101314. ISSN 2352-152X, https://doi.org/10.1016/j.est.2020.101314, https://www.sciencedirect.com/science/article/pii/S2352152X19315890.

[28] Wang Y, Banerjee A, Wehrle L, Shi Y, Brandon N, Deutschmann O, Performance analysis of a reversible solid oxide cell system based on multi-scale hierarchical solid oxide cell modelling, Energy Convers Manag 2019;196:484–96. ISSN 0196-8904, https://doi.org/10.1016/j.enconman.2019.05.099, https://www.sciencedirect.com/science/article/pii/S0196890419306569.

[29] Reznicek E, Braun RJ, Techno-economic and off-design analysis of stand-alone, distributed-scale reversible solid oxide cell energy storage systems, Energy Convers Manag 2018;175:263–77. ISSN 0196-8904, https://doi.org/10.1016/j.enconman.2018.08.087, https://www.sciencedirect.com/science/article/pii/S019689041830952X.

[30] Frank M, Deja R, Peters R, Blum L, Stolten D, Bypassing renewable variability with a reversible solid oxide cell plant, Appl Energy 2018;217:101–12. https://doi.org/10.1016/j.apenergy.2018.02.115

[31] Liu G, Zhao W, Li Z, Xia Z, Jiang C, Kupecki J, Pang S, Deng Z, Li X, Modeling and control-oriented thermal safety analysis for mode switching process of reversible solid oxide cell system, Energy Convers Manag 2022;255:115318. ISSN 0196-8904, https://doi.org/10.1016/j.enconman.2022.115318, https://www.sciencedirect.com/science/article/pii/S0196890422001145.

[32] Xia L, Hua Q, Nižetić S, Sun L, Modelica based modelling and thermodynamic analysis of co-flow and counter-flow solid oxide fuel cell system, Energy Convers Manag 2024;317:118839. ISSN 0196-8904, https://doi.org/10.1016/j.enconman.2024.118839, https://www.sciencedirect.com/science/article/pii/S0196890424007805.

[33] Kim JY, Mastropasqua L, Saeedmanesh A, Brouwer J, Development of thermal control strategies for solid oxide electrolysis cell systems under dynamic operating conditions - hot-standby and cold-start scenarios, Energy 2025;317:134679. ISSN 0360-5442, https://doi.org/10.1016/j.energy.2025.134679, https://www.sciencedirect.com/science/article/pii/S0360544225003214.

[34] Yin R, Chen B, Lee KY, Sun L, System design, operational optimisation and model predictive control of power-to-gas systems based on modelica/simulink co-simulation, Energy 2026;345:140154. ISSN 0360-5442, https://doi.org/10.1016/j.energy.2026.140154, https://www.sciencedirect.com/science/article/pii/S0360544226002562.

[35] Aguiar P, Adjiman CS, Brandon NP, Anode-supported intermediate temperature direct internal reforming solid oxide fuel cell. I: model-based steady-state performance, J Power Sources 2004;138(1):120–36. ISSN 0378-7753, https://doi.org/10.1016/j.jpowsour.2004.06.040, https://www.sciencedirect.com/science/article/pii/S0378775304006950.

[36] Wehrle L, Schmider D, Dailly J, Banerjee A, Deutschmann O, Benchmarking solid oxide electrolysis cell-stacks for industrial Power-to-Methane systems via hierarchical multi-scale modelling, Appl Energy 2022;317:119143. ISSN 0306-2619, https://doi.org/10.1016/j.apenergy.2022.119143, https://www.sciencedirect.com/science/article/pii/S0306261922005190.

[37] Zhu H, Kee RJ, Janardhanan VM, Deutschmann O, Goodwin DG, Modeling elementary heterogeneous Chemistry and electrochemistry in Solid-Oxide fuel cells, J Electrochem Soc Nov 2005;152(12):A2427, https://doi.org/10.1149/1.2116607

[38] VDI e. V. (editor), VDI heat atlas. VDI-Buch. 2nd ed. Springer-Verlag Berlin Heidelberg, 2010, https://doi.org/10.1007/978-3-540-77877-6. ISBN 978-3-540-77876-9. URL. Section C1: Plate Heat Exchangers.

[39] Kandlikar SG, Shah RK, Multipass plate heat exchangers—effectiveness-NTU results and guidelines for selecting pass arrangements, J Heat Transf May 1989;111(2):300–13. https://doi.org/10.1115/1.3250678

[40] Motylinski K, Kupecki J, Numan B, Hajimolana YS, Venkataraman V, Dynamic modelling of reversible solid oxide cells for grid stabilization applications, Energy Convers Manag 2021;228:113674. ISSN 0196-8904, https://doi.org/10.1016/j.enconman.2020.113674, https://www.sciencedirect.com/science/article/pii/S0196890420312000.

[41] Sorrentino M, Pianese C, Model-based development of low-level control strategies for transient operation of solid oxide fuel cell systems, J Power Sources 2011;196(21):9036–45. ISSN 0378-7753, https://doi.org/10.1016/j.jpowsour.2011.01.023, https://www.sciencedirect.com/science/article/pii/S0378775311001017. Fuel Cells Science & Technology 2010.

[42] Uslu U, Zhang B, Energy storages and flexible loads to support large wind power penetration (Master Thesis, Supervisors: Jayakrishnan Radhakrishna Pillai and Sanjay Chaudhary), Aalborg University, Aalborg, Denmark, 2016.

[43] Pukrushpan JT, Stefanopoulou AG, Varigonda S. Control-Oriented model of an integrated fuel cell stack and fuel processor system. In: Proceedings of the American control conference. Boston, MA: American Control Conference; 2004. p. 2024–9.

[44] Anđelković M, Petrović R, Ilić I, Pantović V, Grujić J, Determination of pressure jump dependence and time constants of hydraulic pumps with constant pressure and variable flow, Processes 2024;12(12). ISSN 2227-9717, https://doi.org/10.3390/pr12122761, https://www.mdpi.com/2227-9717/12/12/2761.

[45] Wang Y, Wehrle L, Banerjee A, Shi Y, Deutschmann O, Analysis of a biogas-fed SOFC CHP system based on multi-scale hierarchical modeling, Renew Energy 2021;163:78–87. ISSN 0960-1481, https://doi.org/10.1016/j.renene.2020.08.091, https://www.sciencedirect.com/science/article/pii/S0960148120313367.

[46] Straniero D, Regenerative solid oxide cells (rSOCs) for energy storage applications [Master's thesis], Available at: , Politecnico Di Milano, Milan, Italy, 2017, https://www.politesi.polimi.it/retrieve/a81cb05c-6b6a-616b-e053-1605fe0a889a/Tesi%20rSOC%20StranieroDavide%20CONSEGNA%2007-12%20DEFINITIVA.pdf.

[47] Li J-Q, Chen Y, Ma YB, Kwon J-T, Xu H, Li J-C, A study on the Joule-Thomson effect of during filling hydrogen in high pressure tank, Case Stud Therm Eng 2023;41:102678. ISSN 2214-157X, https://doi.org/10.1016/j.csite.2022.102678, https://www.sciencedirect.com/science/article/pii/S2214157X22009157.

[48] Bensmann B, Hanke-Rauschenbach R, Müller-Syring G, Henel M, Sundmacher K, Optimal configuration and pressure levels of electrolyzer plants in context of power-to-gas applications, Appl Energy 2016;167:107–24. ISSN 0306-2619, https://doi.org/10.1016/j.apenergy.2016.01.038, https://www.sciencedirect.com/science/article/pii/S0306261916300186.

[49] Najjar YSH, Hydrogen safety: the road toward green technology, Int J Hydrog Energy 2013;38:10716–28.

[50] Bell IH, Wronski J, Quoilin S, Lemort V, Pure and pseudo-pure fluid thermophysical property evaluation and the Open-Source thermophysical property library CoolProp, Ind Eng Chem Res 2014;53(6):2498–508. https://doi.org/10.1021/ie4033999, http://pubs.acs.org/doi/abs/10.1021/ie4033999.

[51] Ascencio-Vásquez J, Brecl K, Topič M, Methodology of köppen-Geiger-Photovoltaic climate classification and implications to worldwide mapping of PV system performance, Sol Energy 2019;191:672–85. ISSN 0038-092X, https://doi.org/10.1016/j.solener.2019.08.072, https://www.sciencedirect.com/science/article/pii/S0038092X19308527.

[52] Ministerio de Energía de Chile, Plataforma de exploración solar, 2025, https://solar.minenergia.cl/exploracion [Accessed: 13 August 2025].

[53] Rispoli N, Vitale F, Califano F, Califano M, Polverino P, Rosen MA, Sorrentino M, Constrained optimal design of a reversible solid oxide cell-based multiple load renewable microgrid, J Energy Storage 2020;31:101570. ISSN 2352-152X, https://doi.org/10.1016/j.est.2020.101570, https://www.sciencedirect.com/science/article/pii/S2352152X20302152.

[54] Ebbesen SD, Graves C, Mogensen M, Production of synthetic fuels by Co-Electrolysis of steam and carbon dioxide, Int J Green Energy 2009;6(6):646–60. https://doi.org/10.1080/15435070903372577

[55] Aguiar P, Adjiman CS, Brandon NP, Anode-supported intermediate-temperature direct internal reforming solid oxide fuel cell. II. Model-based dynamic performance and control, J Power Sources 2005;147(1–2):136–47. https://doi.org/10.1016/j.jpowsour.2005.01.017

[56] Zhang W, Xie Y, He H, Long Z, Zhuang L, Zhou J, Multi-physics coupling model parameter identification of lithium-ion battery based on data driven method and genetic algorithm, Energy 2025;314. https://doi.org/10.1016/j.energy.2024.134120, https://www.scopus.com/inward/record.uri?eid=2-s2.0-85211594737&doi=10.1016%2fj.energy.2024.134120&partnerID=40&md5=847fa022f796e8f138f6ff11d512bf73.